

Synthetic lethality of mRNA quality control complexes in cancer

<https://doi.org/10.1038/s41586-024-08398-6>

Received: 26 April 2024

Accepted: 13 November 2024

Published online: 5 February 2025

Open access

 Check for updates

Vivian Prindle^{1,3}, Adam E. Richardson^{1,3}, Kimberly R. Sher^{1,3}, Sarah Kongpachith², Kaitlin Kentala¹, Sakina Petiwala¹, Dong Cheng¹, Deborah Widomski¹, Phuong Le¹, Maricel Torrent¹, Anlu Chen², Stephen Walker¹, Marianne B. Palczewski¹, Diya Mitra¹, Vlasios Manaves¹, Xu Shi², Charles Lu¹, Stephanie Sandoval¹, Zoltan Dezso², F. Gregory Buchanan¹, Daniel Verduzco¹, Brian Biefer¹, Jonathan A. Meulbroek¹, William N. Pappano¹ & Joshua P. Plotnik^{1✉}

Synthetic lethality exploits the genetic vulnerabilities of cancer cells to enable a targeted, precision approach to treat cancer¹. Over the past 15 years, synthetic lethal cancer target discovery approaches have led to clinical successes of PARP inhibitors² and ushered several next-generation therapeutic targets such as WRN³, USP1⁴, PKMYT1⁵, POLQ⁶ and PRMT5⁷ into the clinic. Here we identify, in human cancer, a novel synthetic lethal interaction between the PELO–HBS1L and SKI complexes of the mRNA quality control pathway. In distinct genetic contexts, including 9p21.3-deleted and high microsatellite instability (MSI-H) tumours, we found that phenotypically destabilized SKI complex leads to dependence on the PELO–HBS1L ribosomal rescue complex. PELO–HBS1L and SKI complex synthetic lethality alters the normal cell cycle and drives the unfolded protein response through the activation of IRE1, as well as robust tumour growth inhibition. Our results indicate that PELO and HBS1L represent novel therapeutic targets whose dependence converges upon SKI complex destabilization, a common phenotypic biomarker in diverse genetic contexts representing a significant population of patients with cancer.

The promise of precision medicine relies on the deep understanding of patient genomes and associated vulnerabilities. The CRISPR revolution and genomic profiling technologies, spearheaded by large consortium efforts such as the Cancer Dependency Map (DepMap)⁸ and Cancer Cell Line Encyclopedia^{9,10} have enabled several novel discoveries over the past decade. The integration of these large profiling datasets provides an auspicious opportunity to identify additional synthetic lethal targets among diverse genetic contexts. Synthetic lethality, in which the concurrent loss of two individually non-essential genes results in a loss of cell viability, exemplifies this precision medicine approach in cancer therapy and has shaped much of the clinical landscape of tumour-intrinsic cancer therapies in the twenty-first century.

To explore novel synthetic lethal targets, we developed a digenic CRISPR library of putative synthetic lethal partners¹¹. Previously, in vitro screening confirmed several well-established paralogue synthetic lethal interactions such as *STAG1–STAG2*¹²; we hypothesized that the context of an in vivo CRISPR screen could enable discovery of further therapeutic targets. Here, we began by carrying out an in vivo CRISPR screen in established cell line-derived MDA-MB-231 and NCI-H1299 xenografts (Fig. 1a). In general, we observed strong concordance between putative synthetic lethal pairs tested in MDA-MB-231 and NCI-H1299 (Fig. 1b). However, *IFNB1* and *PELO* sgRNAs were specifically depleted in MDA-MB-231 but not in NCI-H1299 xenograft models (Supplementary Table 1). Whereas NCI-H1299 expresses both *PELO* and *IFNB1*, MDA-MB-231 specifically lacks the *IFNB1* transcript. The lack of

IFNB1 expression in MDA-MB-231 can be explained by the deletion of 9p21.3, which includes the common tumour suppressor gene *CDKN2A*¹³.

Because of the unique, non-paralogue depletion of *PELO* and *IFNB1* in the tumour model with 9p21.3 loss, we hypothesized that *PELO* alone drives the selective anti-proliferative phenotype observed in MDA-MB-231 and that *PELO* dependence may be dictated by collateral loss of a 9p21.3 gene other than *IFNB1*. Human *PELO*—which is evolutionarily conserved through archaea and is most well studied as *dom34* in *Saccharomyces cerevisiae*—is the critical effector protein of the ribosomal rescue and mRNA surveillance complex^{14–16}. *PELO* functions largely in ribosome recycling during no-go and non-stop mRNA decay translation quality control processes, wherein ribosomes accumulate at sites of blunt 3' mRNA cleavage¹⁷ or on poly A tails after skipping of a canonical stop codon due to error or absence^{18,19}. The ribosome rescue complex is comprised of *PELO*, an associated GTPase, *HBS1L* and the ATPase *ABCE1*, which function in concert to split the 80S ribosome and replenish free ribosomal subunit pools for further productive translation^{20–22}.

In support, we confirmed monogenic *PELO* dependency in MDA-MB-231, but not in NCI-H1299, using four independent guide RNAs (Extended Data Fig. 1a–c). Across DepMap²³ models, *PELO* dependency exhibited a strongly selective profile regardless of lineage (Extended Data Fig. 1d). We found that low RNA expression of several genes located on the 9p21.3 locus (*KLHL9*, $R = 0.25$; *FOCAD*, $R = 0.24$; *MTAP*, $R = 0.17$; and *DMRTA1*, $R = 0.16$) strongly correlated with dependency on *PELO*

¹AbbVie, North Chicago, IL, USA. ²AbbVie Bay Area, South San Francisco, CA, USA. ³These authors contributed equally: Vivian Prindle, Adam E. Richardson, Kimberly R. Sher. ✉e-mail: joshua.plotnik@abbvie.com

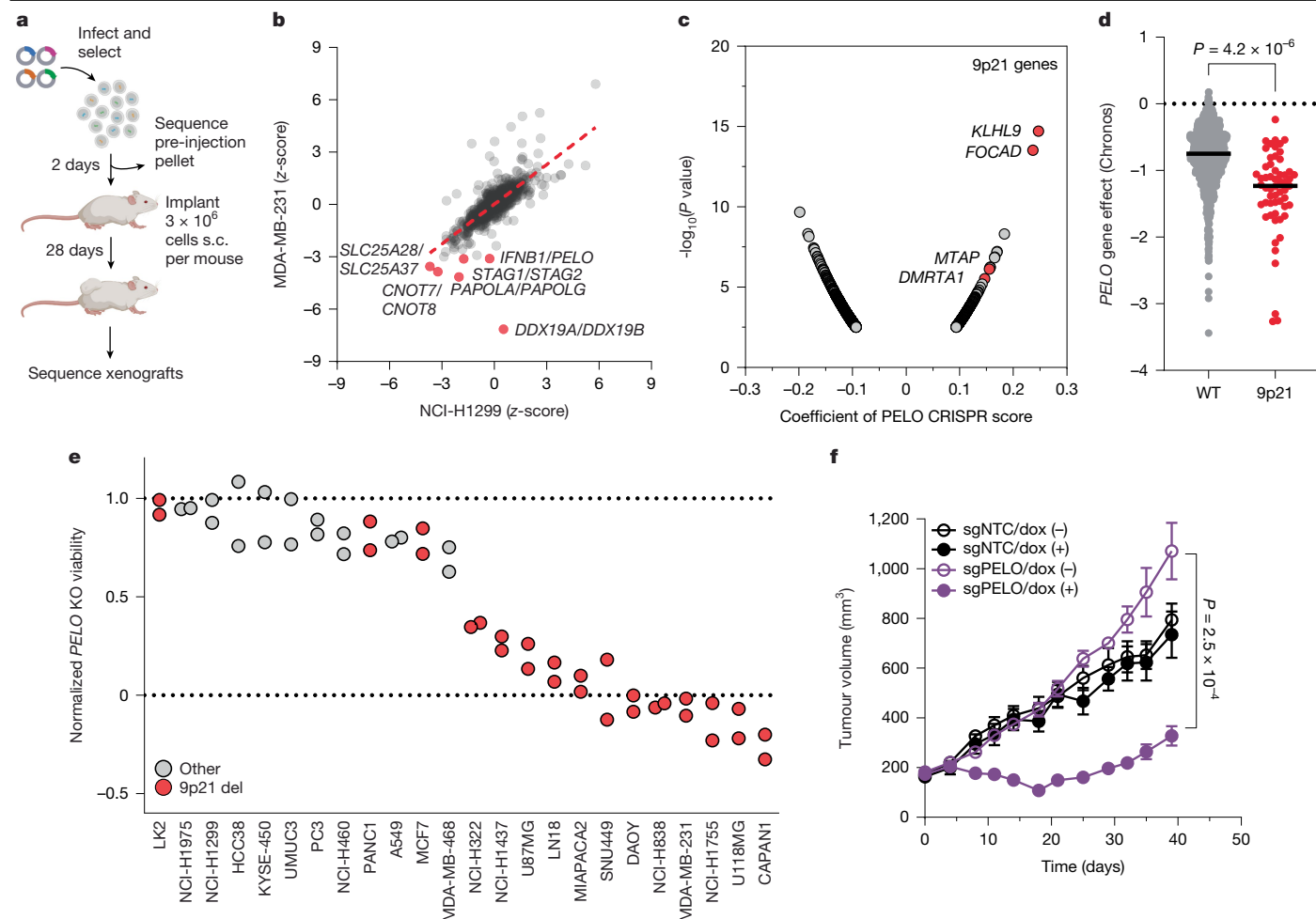


Fig. 1 | PELO is a selective dependency in cancers with 9p21.3 loss. **a**, Design of in vivo CRISPR screen. s.c., subcutaneous. **b**, Digenic CRISPR dropout correlation. In vivo CRISPR results for NCI-H1299 and MDA-MB-231 xenografts at 28 days. Normalized z-scores indicate the change in guide abundance between pre-injection pellet and day 28 after implantation. Selected pairs are highlighted in red. **c**, Pearson correlation of PELO Chronos CRISPR score and gene expression across cell lines in the 23Q4 DepMap release. Top 1,000 correlated genes are shown; genes located on 9p21.3 are highlighted in red. **d**, PELO dependency in 9p21.3-deleted models (9p21 del) are preferentially sensitive across all cancer cell lines available in the 23Q4 DepMap Public Release. Two-tailed Student's *t*-test between mean of wild-type (WT) ($n = 1,043$, mean = -0.795) and

9p21-deleted ($n = 57$, mean = -1.326 ; $P = 4.2 \times 10^{-6}$). **e**, In vitro PELO dependency. Negative control: *B2M* sgRNA. Pan-essential controls: *ABCE1*, *RPA3* and *RAN* sgRNA. Normalized viability at 7 days calculated relative to the negative control and average phenotype of pan-essential genes. Data from $n = 2$ biological replicates calculated as average of $n = 3$ technical replicates per cell line. KO, knockout. **f**, In vivo PELO dependency. Growth of size-matched (200 mm^3) xenografted 9p21-deleted MIAPACA2 tumours with doxycycline (dox)-inducible sgRNA targeting *PELO* (sgPELO) or non-targeting sgRNA (NTC). Doxycycline (625 mg kg^{-1}) chow was administered ad libitum. Data are mean \pm s.e.m. of $n = 8$ mice. Two-tailed Student's *t*-test between groups on day 40; $P = 2.5 \times 10^{-4}$.

(Fig. 1c). Two-group analysis of the large 9p21.3 deep deletion encompassing all genes located between a boundary established by *DMRTA1* and *MLL3* confirmed a significant association with PELO dependency ($n = 57$, $P = 4.2 \times 10^{-6}$; Fig. 1d).

We next investigated the effect of *PELO* knockout in a panel of cancer cell lines ($n = 24$) selected by large 9p21.3 deletion status. Overall, *PELO* loss showed consistent selectivity and robust loss of viability among cell models harbouring large 9p21.3 loss ($n = 15$; Fig. 1e and Extended Data Figs. 1e and 2a). Highlighting the specificity of *PELO* dependence for 9p21.3 status, knockout in four normal cell lines from different tissues did not result in viability changes (Extended Data Fig. 2b). To solidify this genetic relationship between 9p21.3 and *PELO* in vivo, we selected MIAPACA2, a pancreatic cancer cell line model with a naturally occurring 9p21.3 deletion to generate a polyclonal inducible-knockout system. Induction of *PELO* knockout in established MIAPACA2 xenografts resulted in significant tumour growth inhibition of 74% ($P = 2.5 \times 10^{-4}$; Fig. 1f). Although we observed robust tumour growth inhibition, we observed only a 60% partial reduction in *PELO*

protein levels throughout the study (Extended Data Fig. 1f,g). The regression and return of tumour growth correlates with quantifiable return of *PELO* protein levels. These data identify and validate *PELO* as a bona fide vulnerability in tumours with 9p21.3 loss.

To identify the causal synthetic lethal interactor with *PELO*, we generated a clonal NCI-H1299 *PELO*^{-/-} model with no discernable growth rate differences compared with the parent (Extended Data Fig. 2c). We generated a single guide RNA (sgRNA) library (Supplementary Table 2) containing associated ribosomal and translational ontological pathways^{24,25}, UniProt-predicted *PELO*-interacting proteins²⁶, and all genes commonly deep deleted on 9p21.3 (Fig. 2a). Parental and *PELO*-knockout cells were propagated with library for two weeks and then sequenced for sgRNA representation (Fig. 2b). As DepMap suggested a genetic interaction between *PELO* and a gene located within the boundary of the 9p21.3 chromosome deletion, we first looked at representation across genes frequently deleted within the 9p21.3 loci. Of candidate 9p21.3 genes ($n = 21$), only sgRNAs targeting *FOCAD* were significantly and specifically depleted in the *PELO*-knockout background

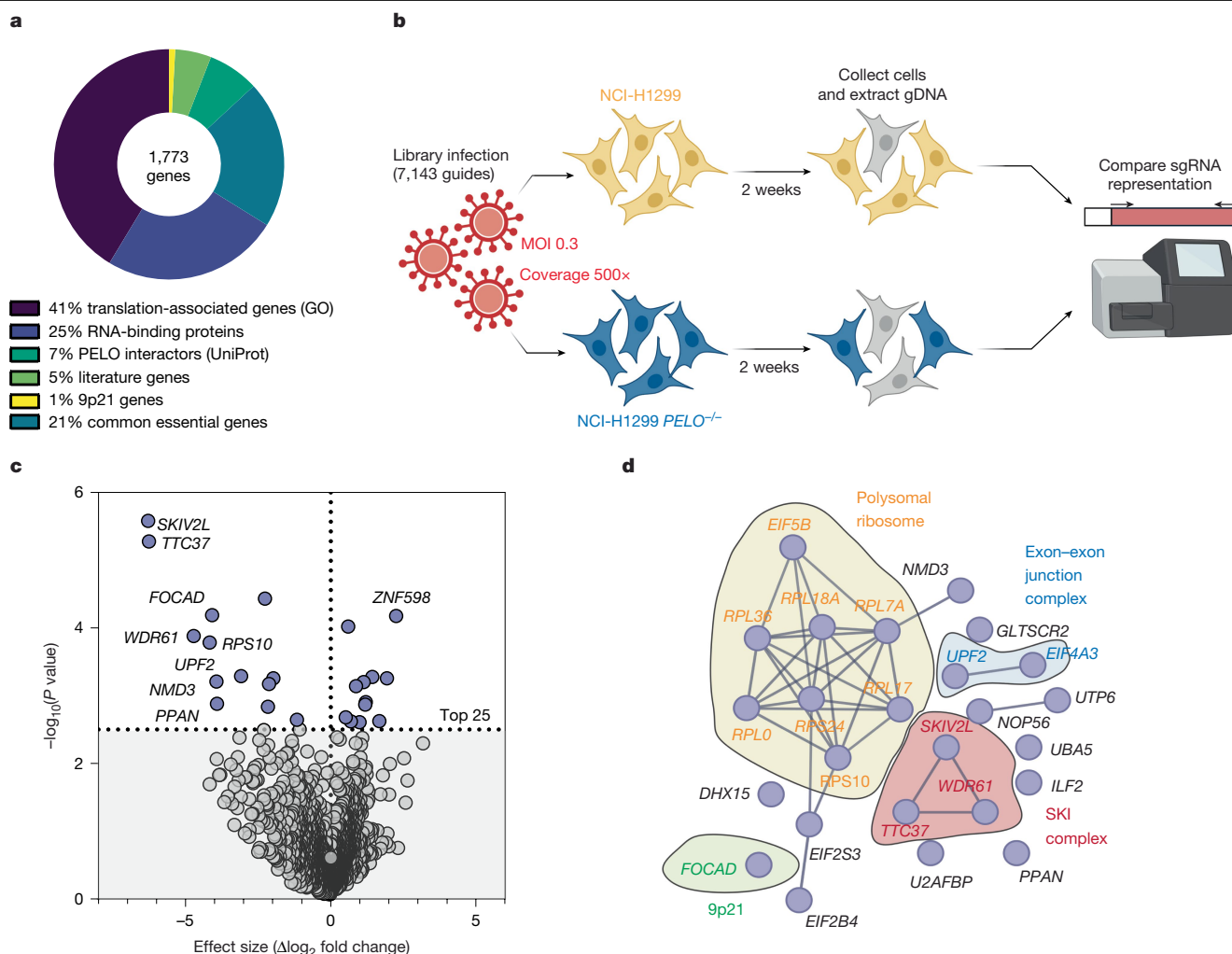


Fig. 2 | *FOCAD* deletion dictates 9p21 synthetic lethality. **a**, *PELO* SL-ID library composition. GO, gene ontology. **b**, Experimental design for *PELO* SL-ID screen. Library infected at a multiplicity of infection (MOI) of approximately 0.3, with approximately 500 \times representation per sgRNA. gDNA, genomic DNA. **c**, Results of the *PELO* SL-ID screen, with genes of interest labelled. Effect size calculated

from $n = 3$ independent replicates. Two-tailed Student's *t*-test followed by Benjamini–Hochberg correction for multiple-hypothesis testing. *WDR61* is also known as *SKIC8*. **d**, StringDB physical subnetwork analysis of the top 25 most significant hits from *PELO* SL-ID in **c**. Enriched complexes and 9p21.3 genes are circled.

($P = 5.7 \times 10^{-3}$; Extended Data Fig. 4a), identifying *FOCAD* deletion on 9p21.3 as the driver synthetic lethal partner dictating *PELO* dependency.

The function of *FOCAD* remains largely unknown, but germline deletions and an increased incidence of *FOCAD* mutations in familial colorectal and breast cancers suggest that it may have a role as a putative tumour suppressor^{27,28}. Although we expected to find a gene within the 9p21.3 boundary, we were surprised to also observe that both *SKIV2L* (also known as *SKIC2*) and *TTC37* (*SKIC3*) exhibited a greater significance than *FOCAD* in the NCI-H1299 *PELO*^{-/-} cell line (Fig. 2c). Functional protein networks identified *SKIV2L*, *TTC37* and a third hit, *WDR61*, as core components of the SKI complex (SKIC) (Fig. 2d), which is responsible for mRNA extraction from ribosomes permitting exonuclease activity and turnover of damaged mRNAs^{29,30}. Of note, recent reports highlight germline pathogenic *FOCAD* mutations in paediatric liver cirrhosis and suggest that *FOCAD* functions as a critical scaffold protein to maintain the stability of the core SKIC members, *SKIV2L* and *TTC37*³¹. Together, these data present a strong genetic link between *FOCAD*, SKIC, and *PELO* in human cancers and illuminate the synthetic lethal interaction between two independent complexes.

To test the relationship between *FOCAD* and SKIC in cancer, we returned to DepMap and tested whether *PELO* dependency correlated to the loss of SKIC proteins across the proteome. In agreement with the

PELO synthetic lethal ID (SL-ID) screen, low protein expression of *SKIV2L* and *TTC37* ($R = 0.46$ and 0.45 respectively) were top predictors of *PELO* dependency, followed by low expression of the SKIC accessory proteins *FOCAD* ($R = 0.28$) and *AVEN* ($R = 0.24$, Fig. 3a). *TTC37* and *SKIV2L* protein levels significantly correlate across both *FOCAD* (9p21.3)-deleted cell lines ($n = 57$; Fig. 3b,c) and tumours ($n = 36$; *SKIV2L*, $P = 4.5 \times 10^{-6}$; *TTC37*, $P = 1.8 \times 10^{-7}$; Fig. 3d,e), supporting the role of *FOCAD* in promoting *SKIV2L* stability. In addition, *SKIV2L* and *TTC37* expression at the protein level exhibit remarkable correlation in both cell lines ($n = 375$, $r = 0.94$) (Extended Data Fig. 3a) and tumours ($n = 1022$, $R^2 = 0.75$) (Fig. 3d,e and Supplementary Table 3), indicating that *SKIV2L* and *TTC37* may act as requisite post-transcriptional stability partners.

We next generated a panel of clonal isogenic models in NCI-H1299 cells with knockout of *SKIV2L*, *TTC37*, *FOCAD* or *AVEN* and probed for the remaining SKIC proteins. In all SKIC isogenic models, we observed destabilization of the non-edited members compared with basal expression, with the exception of *WDR61* (Fig. 3f). We suspect that the incorporation of *WDR61* in the co-transcriptional PAF complex may protect it from destabilization upon collapse of SKIC³². Notably, the core enzymatic SKIC proteins *SKIV2L* and *TTC37* were depleted across all SKIC knockouts, whereas *FOCAD* and *AVEN* were interdependent upon each other, suggesting that the incorporation of *FOCAD* and *AVEN*

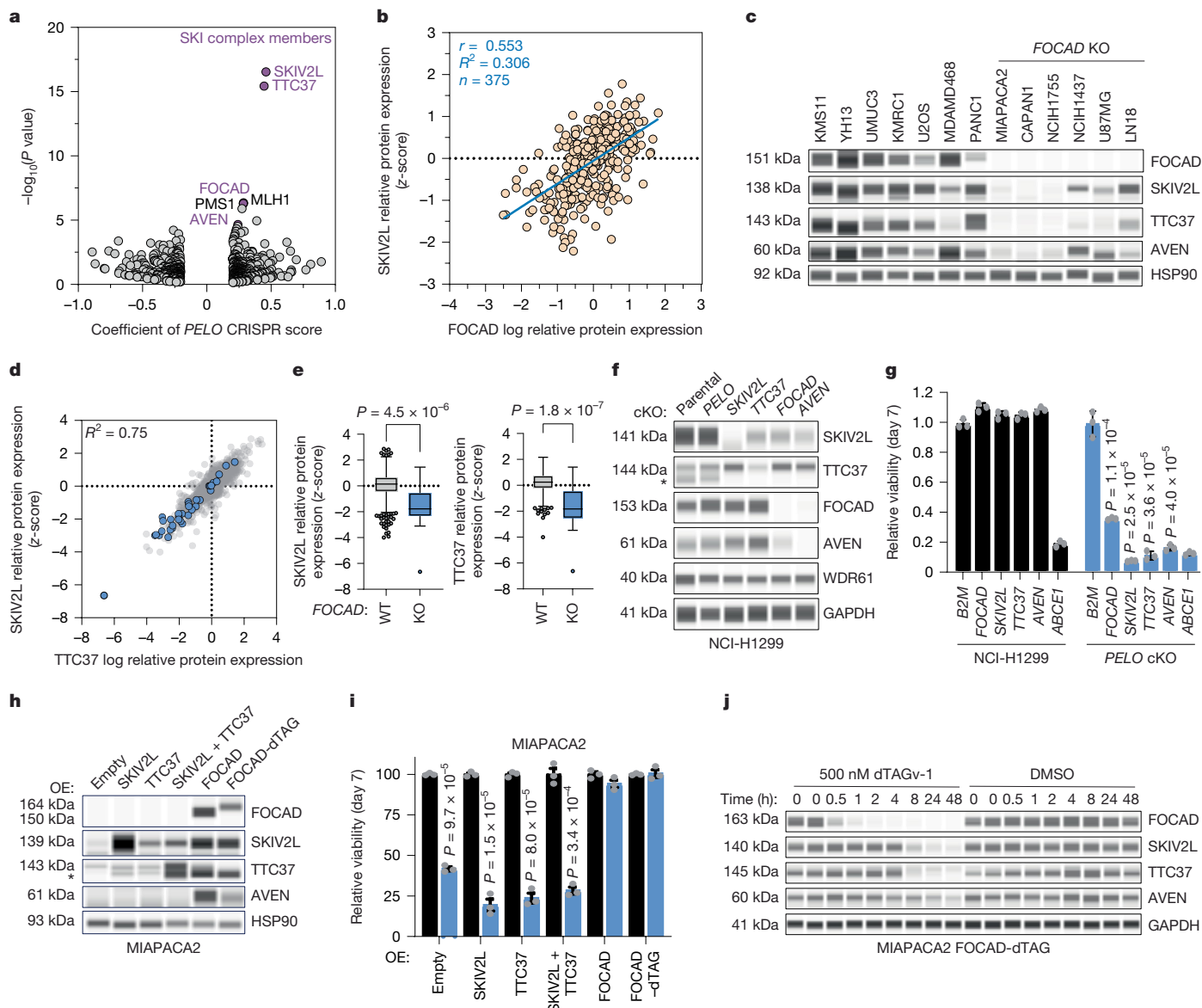


Fig. 3 | SKIc is lost in cancer and drives PELO dependency. **a**, Pearson correlation between *PELO* Chronos CRISPR score and whole-proteome data from cell lines ($n = 375$) available in the 23Q4 DepMap release. Top 1,000 correlated proteins shown, SKIc proteins are labelled in purple. Two-tailed Student's *t*-test. **b**, FOCAD and SKIV2L protein levels across cell lines analysed in the 23Q4 DepMap release. Pearson's $r = 0.553$; $n = 375$. **c**, Immunoblot of SKIc proteins in FOCAD homozygous deletion (FOCAD KO) and FOCAD-expressing cell lines. **d**, Correlation of SKIV2L and TTC37 protein expression in tumours. Data from the PanCancer Clinical Proteomic Tumor Analysis Consortium (CPTAC) cohort ($n = 1,022$). Models with FOCAD homozygous deletion are highlighted in blue. Pearson's coefficient of determination (R^2) = 0.75. **e**, Relative SKIV2L and TTC37 protein expression in tumours with (KO, $n = 36$) and without (WT, $n = 986$) FOCAD homozygous deletion. Two-tailed Student's *t*-test between two groups; SKIV2L, $P = 4.5 \times 10^{-6}$; TTC37, $P = 1.8 \times 10^{-7}$. In box plots, the centre line is the median, box edges delineate 25th and 75th percentiles and whiskers

extend to 10th and 90th percentiles; data outside whiskers are shown as individual points. **f**, Immunoblot of SKIc isogenic clonal knockout (cKO) NCI-H1299 cell lines. Asterisk denotes TTC37-specific bands. **g**, Validation of PELO and SKIc synthetic lethality. Relative viability of parental or *PELO* cKO NCI-H1299 cells following acute knockout of indicated SKIc gene or *B2M* negative control. FOCAD, $P = 1.1 \times 10^{-4}$; SKIV2L, $P = 2.5 \times 10^{-5}$; TTC37, $P = 3.6 \times 10^{-5}$; AVEN, $P = 4.0 \times 10^{-5}$. **h**, Reconstitution of SKIc. Immunoblot in MIAPACA2 cells with exogenous expression of indicated SKIc proteins. **i**, Functional rescue of PELO dependency by overexpression (OE) of indicated proteins. Relative viability was assessed on day seven and normalized to *B2M* sgRNA control. **j**, FOCAD-driven SKIc stability. Time course of SKIV2L, TTC37, FOCAD and AVEN protein expression following treatment with 500 nM dTAG-v1 (inducible degron tag). Data are mean \pm s.e.m. Two-tailed Student's *t*-test. Representative data shown as $n = 3$ independent biological replicates (**g**, **i**) or representative data shown from one of two independent replicates (**c**, **f**, **j**).

into the core SKIc is necessary for stability but alone is not sufficient for functional activity (Fig. 3f).

As SKIc destabilization was observed across all derived isogenic models, we next asked whether PELO would be synthetic lethal with deletion of any SKIc member. Consistently across orthogonal methods, loss of any SKIc member (SKIV2L, $P = 2.5 \times 10^{-5}$; TTC37, $P = 3.6 \times 10^{-5}$; FOCAD, $P = 1.1 \times 10^{-4}$; AVEN, $P = 4.0 \times 10^{-5}$; or WDR61) conferred selective

anti-proliferative phenotypes in PELO-deficient, but not wild-type, NCI-H1299 cells (Fig. 3g and Extended Data Fig. 4g, h); this was confirmed in a HAP1 SKIV2L^{-/-} isogenic pair ($P = 9.9 \times 10^{-7}$; Extended Data Fig. 4d, e). We also noted an upregulation in the basal machinery of the ribosomal rescue complex (PELO, HBS1L and ABCE1) in the SKI deficient isogenic models, hinting at increased reliance on PELO function (Extended Data Fig. 4c). In FOCAD (9p21.3)-deleted MIAPACA2 cells, SKIc rescue via

exogenous SKIV2L, TTC37 or dual SKIV2L and TTC37 co-expression ($P = 1.5 \times 10^{-5}$, 8.0×10^{-5} or 3.4×10^{-4} , respectively) was insufficient to protect cells from PELO dependency, suggesting that the SKIc function requires more than just the core helicase for rescue complex activity. Solely upon re-expression of FOCAD did we observe full complex and functional rescue of PELO dependency (Fig. 3h,i). To confirm the results from FOCAD depletion experiments regarding the loss of associated SKIc members (Fig. 3f), we generated a MIAPACA2 model with FOCAD under the inducible control of a degron tag (dTAG)³³. Treatment with 500 nM of dTAG-v1 depleted FOCAD protein levels within four hours. Following FOCAD degradation, levels of SKIV2L, TTC37 and AVEN protein decreased by 8 h, reaching a maximum by 2 days (Fig. 3j). Consistent with a mechanism through which loss of protein complex subunits leads to posttranslational quality control³⁴, we observed no meaningful downregulation in SKIc RNA levels up to 24 h (FOCAD, $P = 0.99$; TTC37, $P = 0.14$; SKIV2L, $P = 0.17$; AVEN, $P = 0.03$; Extended Data Fig. 4f).

As our data support the notion that PELO and SKIc synthetic lethality can occur regardless of which SKIc member is lost, we rationalized that in addition to 9p21.3, other chromosomal deletions may present additional translational opportunity. Although the homozygous deletion of *FOCAD* (9p21.3) is the most frequently deleted SKIc member (4% PanCan), The Cancer Genome Atlas (TCGA) database highlights mutually exclusive homozygous deletions of *SKIV2L*, *TTC37*, *AVEN* or *WDR61* (also known as *SKIc8*) in another 2% of cancers (Extended Data Fig. 5a,b). Furthermore, SKIc members are found to be mutated across multiple tumour types (Extended Data Fig. 6f). All identified mutations are characterized as variants of unknown significance (Supplementary Table 4); however, several cancer-associated missense and nonsense SKIV2L (R483C, R756* and R510*) and TTC37 (R570* and R1503C) mutations are causal in patients with trihepatoenteric syndrome (THES)^{35–37}. To validate whether overlapping cancer and THES missense mutations may also drive a synthetic lethal interaction with PELO, we attempted to rescue PELO dependency by exogenous expression of either SKIV2L wild type or R483C in the NCI-H1299 *SKIV2L*^{−/−} model. Unexpectedly, and mechanistically divergent from *SKIV2L* knockout, stable expression of both forms of SKIV2L increased TTC37 protein levels. However, consistent with the characterized pathogenicity of R483C in THES, stable expression of this mutant phenocopied SKIV2L knockout, suggesting R483 is critical for enzymatic function but not stability of SKIV2L (Extended Data Fig. 5c–e). Together, these data support a hypothesis in which nonfunctional SKIc can be attained via multiple genomic alterations, converging on a synthetic lethal relationship with PELO.

Outside of *FOCAD* (9p21.3) and SKIc loss, PELO dependency best correlated to low protein expression of MLH1 and PMS1, two frequently mutated genes that permit a hypermutated phenotype characteristic of high microsatellite instability (MSI-H) (Fig. 3a). MSI-H tumours account for 3.8% of all cancers and up to 15% of colorectal, uterine and ovarian tumours³⁸, and MSI-H status is mutually exclusive with *FOCAD* (9p21.3) deep deletion in major microsatellite instability lineages (bowel, uterine, ovarian and lymphoid), suggesting that MSI-H and *FOCAD* deletion may converge on a common biomarker (Extended Data Fig. 6b). Proteomics across MSI-H cancer cell lines previously identified low expression of both SKIV2L and TTC37 as compared to MSS models³⁹, indicating that our observed correlation between PELO dependence and the MSI-H cell state may also hinge on SKIc stability.

Consistent with this hypothesis, we validated a specific dependency for PELO in the MSI-H cell lines HCT-116, RKO, DLD-1 and MFE-319 (Extended Data Fig. 6a), and DepMap showed higher PELO dependence in MSI-H compared with microsatellite stable (MSS) cell model ($n = 61$; bowel, $P = 4.0 \times 10^{-13}$; uterine, $P = 2.8 \times 10^{-3}$; ovary, $P = 2.0 \times 10^{-3}$; and lymphoid, $P = 0.03$; Extended Data Fig. 6b). We next explored whether the loss of SKIV2L and TTC37 in MSI-H cells mimicked the degree of SKIc loss seen in *FOCAD* (9p21.3) homozygous-deleted models. As expected, both MSI-H cell models ($n = 6$) and primary tumours (colorectal, $n = 20$; and uterine, $n = 27$) exhibited lower abundance of SKIV2L and TTC37

than MSS, phenocopying *FOCAD* (9p21.3)-deleted models but presenting independent of FOCAD protein levels (Extended Data Fig. 6c–e). Unlike the MSI-H synthetic lethal target WRN⁴⁰, PELO dependency does not appear to be dictated by TP53 status (Extended Data Fig. 6g), as highlighted by the DLD-1 *TP53* wild type, MSI-H colorectal cancer model (Extended Data Fig. 6h,i). Together, these data identify MSI-H tumours as a second biomarker-driven population with destabilized SKIc and dependence on *PELO* gene function. Loss of the SKIc, either through *FOCAD* (9p21.3) deletion, deletion of other SKIc members, mutation or MSI-H status converge on a common proteomic biomarker that is sufficient to drive a synthetic lethal dependency on PELO and strengthens the potential translational impact.

We next sought to determine the cellular mechanisms by which PELO and SKIc synthetic lethality resulted in the observed anti-proliferative phenotype. To address this, we carried out orthogonal high-content and flow cytometric panels in two sets of isogenic cell lines, NCI-H1299 with or without SKIV2L expression and MDA-MB-231 with or without FOCAD expression for three days after *PELO* knockout. We observed a marked loss of EdU incorporation, indicating a collapsed S-phase specifically in conditions in which both PELO and SKIc were lost (NCI-H1299 *SKIV2L*^{−/−}, $P = 2.2 \times 10^{-13}$; and MDA-MB-231 *FOCAD* deletion, $P = 1.2 \times 10^{-11}$; Fig. 4a,b). The collapse of S-phase was confirmed by propidium iodide and EdU staining measured by flow cytometry in the same model set (Extended Data Fig. 7a,b). Cell cycle arrest differed between the NCI-H1299 and MDA-MB-231 isogenic models, with pauses in G1 and G2 respectively, suggesting there may be cell-specific factors that dictate the PELO and SKIc synthetic lethal phenotype (Fig. 4c). Further staining for cell viability markers did not quantifiably identify an early apoptotic response, consistent with a primary cell arrest phenotype (Extended Data Fig. 7c). By 120 h, both NCI-H1299 *SKIV2L*^{−/−} and MIAPACA2 show nearly a quarter of cells undergoing late apoptosis as measured by annexin V positivity (Extended Data Fig. 7d). These data support a model in which PELO and SKIc synthetic lethality initially forgoes normal S-phase progression, eventually leading towards late apoptosis and cell death.

We next utilized the SKIc-compromised MIAPACA2 model to assess global transcriptional changes after induction of *PELO* knockout. Analysis of differentially regulated pathways demonstrates consistent and significant upregulation of gene expression programmes driven by NF- κ B, p53 and unfolded protein response (UPR) pathways (Fig. 4d and Extended Data Fig. 7e). Several reports have highlighted an intricate relationship between the role of PELO and SKIc in no-go mRNA decay and the activity of the UPR pathway^{41,42}. PELO loss in the MIAPACA2 model induced key UPR genes at the protein level at 48 h, before cell cycle and proliferation defects, and triggered downstream activation of p38 and JNK pathways. Concomitant with CHOP upregulation, we also observed an increase in cleaved PARP and p21 (Fig. 4e). To validate the MIAPACA2 transcriptomic and proteomic validation, we returned to our NCI-H1299 isogenic system and endogenous *FOCAD* (9p21.3)-deleted cell lines to assess changes in UPR pathway genes and the phosphorylated JNK (pJNK) pathway. By inducing PELO and SKIc synthetic lethality we observed a consistent and robust increase in IRE1 α , CHOP and pJNK protein levels across several models (Fig. 4f and Extended Data Fig. 7f), strongly suggesting that the induction of UPR is a consequence of dual loss of PELO and SKIc.

As IRE1 α activity is driven by dimerization⁴³, we tested whether increased IRE1 α protein levels were sufficient to drive mechanistic activation upon induction of synthetic lethality. We observed a tenfold induction ($P = 1.2 \times 10^{-6}$) of stained foci in the *PELO*-deleted cells compared with the negative control (Fig. 4g,h). IRE1 α was also upregulated in a panel of twelve 9p21.3-homozygous-deleted ($n = 5$) or wild-type ($n = 7$) models (Extended Data Fig. 7g). Together, the robust PELO and SKIc synthetic lethality phenotype appears to activate a UPR signalling cascade through IRE1 α and is associated with dysfunctional normal cell cycle progression through S-phase.

Structural insights from yeast suggest that PELO and its requisite binding partner HBS1L work in concert with ABCE1 to comprise

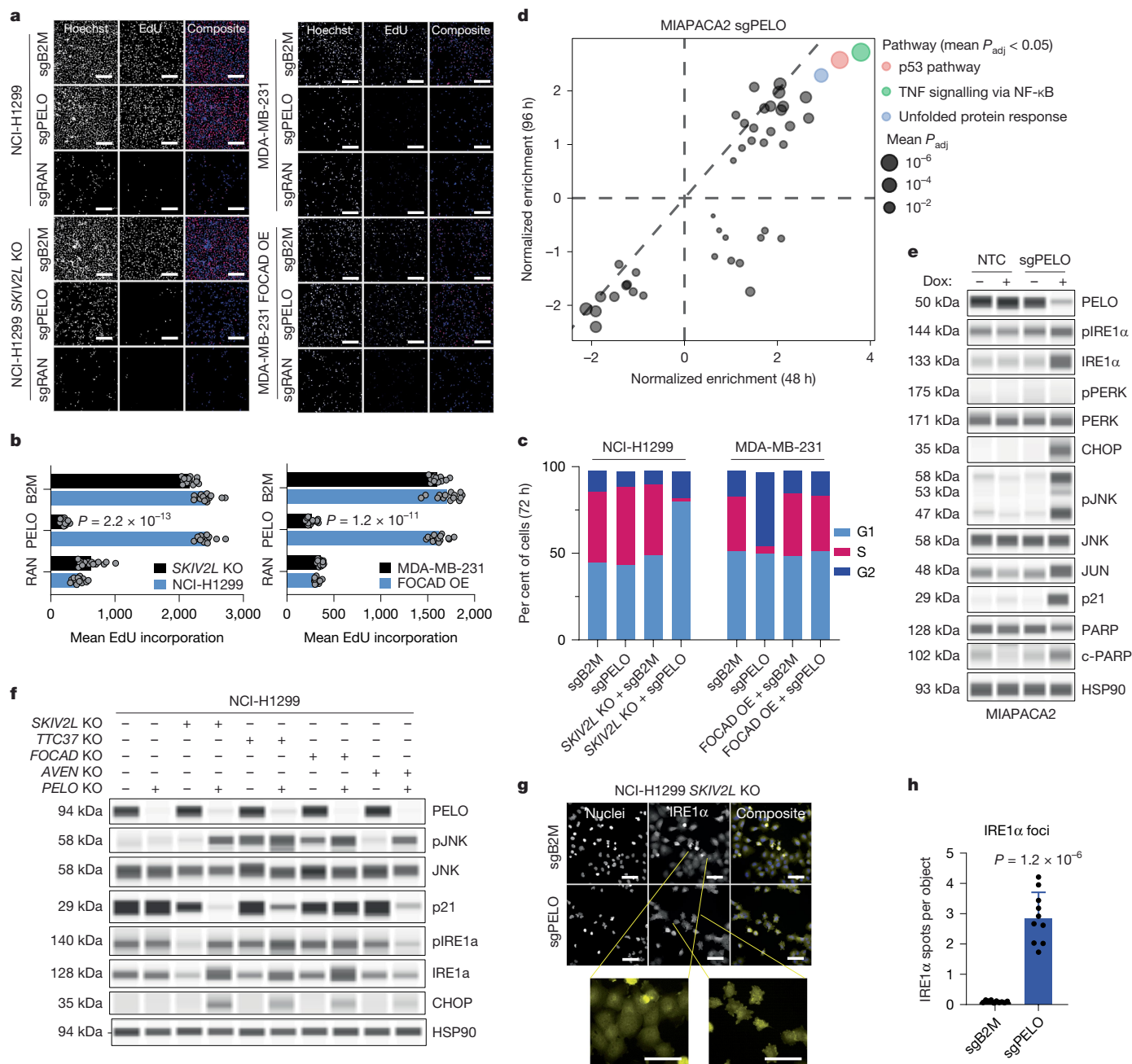


Fig. 4 | PELO and SKIc synthetic lethality induces cell cycle arrest and UPR.

a, Representative high-content images of Hoechst and Edu staining in isogenic SKIc models 72 h after transfection of sgRNA targeting *B2M* (sgB2M), *PELO* (sgPELO) or *RAN* (sgRAN). Scale bars, 200 μ m. **b**, Mean average Edu incorporation in NCI-H1299 with or without SKIV2L expression (left) and MDA-MB-231 with or without FOCAD overexpression (right) 72 h after transfection with sgB2M, sgPELO or sgRAN. Data are mean \pm s.e.m. of $n = 2$ independent biological replicates, $n = 7$ images per replicate. Two-tailed Student's *t*-test for sgPELO with SKIc (NCI-H1299 or FOCAD OE) versus without SKIc (SKIV2L KO or MDA-MB-231): NCI-H1299, $P = 2.2 \times 10^{-13}$; MDA-MB-231, $P = 1.2 \times 10^{-11}$. **c**, Cell cycle analysis 72 h after infection with sgB2M or sgPELO. G1, S and G2 phases gated by Edu and PI intensity. **d**, Differentially regulated pathways in MIAPACA2 after doxycycline-induced sgPELO expression. Size of bubble indicates average

adjusted P value (P_{adj}); P value estimation based on an adaptive multi-level split Monte Carlo scheme. $n = 3$ independent replicates per time point. **e**, Validation of sgPELO RNA sequencing results. Samples were collected 48 h after sgPELO infection and protein extracts were blotted with indicated antibodies. **c**-PARP, cleaved PARP; pIRE1 α , phosphorylated IRE1 α . **f**, UPR pathway regulation in NCI-H1299 SKIc isogenic models transfected with sgB2M or sgPELO. Samples were collected at 48 h. **g**, High-content imaging of IRE1 α foci in the NCI-H1299 SKIV2L-knockout cell line. Images were collected 48 h after sgB2M or sgPELO treatment. Scale bars, 400 μ m. **h**, Quantification of IRE1 α foci per object from **g**, 48 h after sgB2M or sgPELO transfection of SKIV2L-knockout NCI-H1299 model. Five images were acquired from two independent biological replicates. Data are mean \pm s.e.m. Two-tailed Student's *t*-test, $P = 1.2 \times 10^{-6}$. Representative data shown from one of two independent replicates (**e**, **f**).

the functional rescue complex⁴⁴. We thus postulated that HBS1L may phenocopy the synthetic lethality of PELO in SKIc-deficient tumour models. Although HBS1L dependency in DepMap appears less severe across most models as compared to PELO, dependency

on the two proteins significantly correlates across the dataset, and HBS1L dependency correlates with the expression of 9p21.3 genes and protein levels of SKIc (Extended Data Fig. 8a–c). *HBS1L* knockout across a panel comprising 11 SKIc wild-type ($n = 6$) or compromised

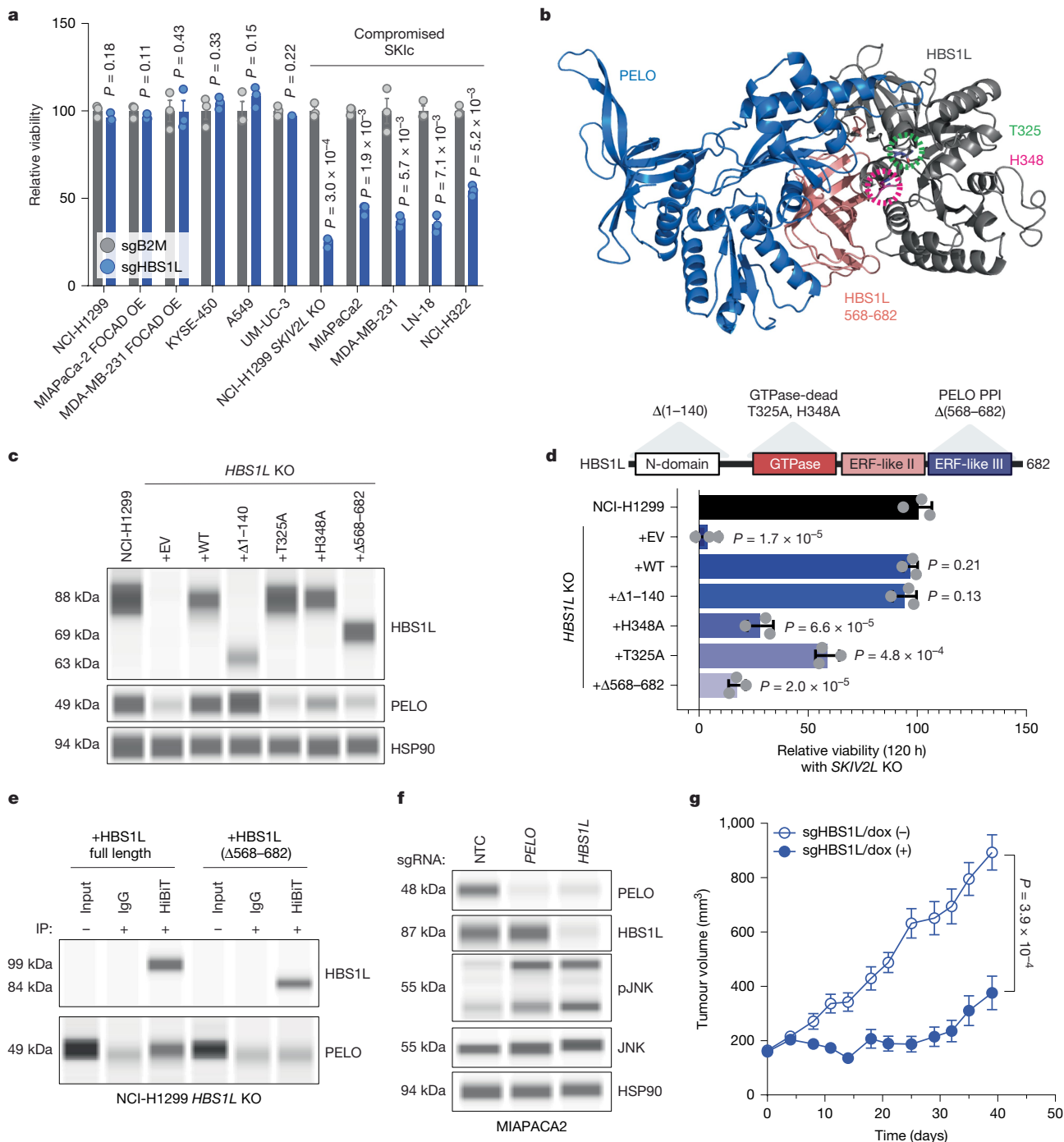


Fig. 5 | *HBS1L* is a synthetic lethal target in cancers with *SKIc* loss. **a, *HBS1L* knockout in a panel of cell lines. Relative viability of sgHBS1L or sgB2M cells at day 7. Data are mean \pm s.e.m. of $n = 3$ independent biological replicates. **b**, Model of the PELO–HBS1L complex, adapted from Protein Data Bank ID 5LZZ. PELO is shown in blue, HBS1L is in grey. Key HBS1L residues (568–682) along the PELO interaction surface are shown in salmon. GTPase catalytic residues T325 and H348 are circled with green and pink dotted lines, respectively. **c**, Validation of a stable NCI-H1299 sgHBS1L model (*HBS1L* KO) and HBS1L rescue constructs. **d**, Functional characterization of HBS1L. Data shown from $n = 3$ independent biological replicates. EV, empty vector, $P = 1.7 \times 10^{-5}$; wild type, $P = 0.21$; $\Delta 1-140$,**

$P = 0.13$; H348A, $P = 6.6 \times 10^{-5}$; T325A, $P = 4.8 \times 10^{-4}$; $\Delta 568-682$, $P = 2.0 \times 10^{-5}$. **e**, Co-immunoprecipitation of full-length HBS1L and HBS1L ($\Delta 568-682$) and PELO. Representative image of a single experiment from two independent biological replicates. **f**, Immunoblot for validation of the inducible sgHBS1L model. Experiment performed once. **g**, In vivo HBS1L dependency. Growth of size-matched (200 mm³) implanted doxycycline-inducible sgHBS1L MIAPaCa2 model. Doxycycline (625 mg kg⁻¹) chow was administered ad libitum. Data show mean \pm s.e.m. of $n = 8$ mice per group. P-value calculated at study end, $P = 3.9 \times 10^{-4}$. Two-tailed Student's *t*-test (**a**, **d**, **g**).

cell lines ($n = 5$) elicited selective HBS1L dependency in the context of SKIc loss (Fig. 5a and Extended Data Fig. 8d–f). Our data suggest that HBS1L is a second vulnerability in SKIc-deficient models, and that it probably acts through regulation of the ribosome rescue complex.

The structure of the mammalian PELO–HBS1L interface⁴⁵ was used to map putative regions of HBS1L that are responsible for the synthetic lethal relationship with the SKIc (Fig. 5b). We generated a *HBS1L*^{-/-} model in NC-H1299 cells and exogenously expressed several *HBS1L*-mutant constructs (Fig. 5c). Consistent with previous reports^{46,47}, loss of HBS1L

protein significantly destabilized PELO protein expression (Fig. 5c). We observed a lack of PELO protein and functional rescue in GTPase-dead (T325A, $P = 4.8 \times 10^{-4}$; or H348A, $P = 6.6 \times 10^{-5}$) and C-terminal-deleted HBS1L ($\Delta 568-682$, $P = 2.0 \times 10^{-5}$) constructs. Rescue occurred only with wild-type and N-terminus deleted ($\Delta 1-140$) HBS1L constructs ($P = 0.21$ and 0.13 , respectively), consistent with a hypothesis in which HBS1L phenocopies PELO–SKIC synthetic lethality by maintaining PELO protein stability (Fig. 5c,d). To confirm the requirement of the C terminus of HBS1L for PELO, we used a HiBIT-tagged HBS1L to immunoprecipitate HBS1L and test for interaction with PELO. Full-length, wild-type HBS1L maintained the interaction with PELO, whereas the C-terminal truncated mutant HBS1L ($\Delta 568-682$) ablated binding with PELO, demonstrating the critical nature of the interaction surface for HBS1L and PELO complexing and function (Fig. 5e). Together, these results highlight the requirement for both GTPase activity and the PELO-interacting surface of HBS1L for functional ribosome rescue complex activity.

Finally, we explored the functional response to *HBS1L* knockout in an inducible MIAPACA2 cell line model. Consistent with our previous observations, we observed PELO protein loss and pJNK activation at 48 h after *HBS1L* knockout (Fig. 5f). Induction of *HBS1L* knockout in established MIAPACA2 xenografts resulted in concomitant loss of HBS1L and PELO upon doxycycline treatment and 70% tumour growth inhibition ($P = 3.9 \times 10^{-4}$), phenocopying the total growth inhibition of the MIAPACA2 inducible *PELO*-knockout xenografts (Fig. 5g and Extended Data Fig. 8g,h). These data demonstrate that PELO destabilization through HBS1L depletion likely functionally drives the observed anti-proliferative phenotype, and that incomplete PELO inhibition is sufficient to confer a synthetic lethal relationship with SKIC.

Discussion

These studies identify a novel synthetic lethal interaction between the PELO–HBS1L ribosome rescue complex and the SKIC involved in RNA decay, highlighting PELO and HBS1L as potential high-value therapeutic targets to address cancers with *FOCAD* (9p21.3) deletion, MSI-H and other genetic modes of SKIC destabilization. The interaction between the PELO–HBS1L and SKI complexes are reminiscent of other non-paralogue synthetic lethal relationships (such as PARP1–PARP2 and BRCA1–BRCA2) whereby loss of one cellular function requires another process to escape lethality. Although we propose two new therapeutic targets for the development of treatments against SKIC-deficient cancers, more work is needed to understand the full translational effect of PELO and HBS1L. In this work, we highlight homozygous deletions of SKIC members (most frequently *FOCAD*) and MSI-H as mutually exclusive contexts in which the SKIC is destabilized. However, several areas require additional investigation. First, the causal mechanism of SKIC loss in MSI-H tumours is unknown. Second, we do not fully understand how models with heterozygous loss of SKIC members destabilize the SKIC as we observe several 9p21.3 heterozygous-deleted models lacking SKIC protein expression that are sensitive to PELO and HBS1L depletion. Whether these models exhibit loss of heterozygosity or other features that destabilize SKIC remains unknown. Lastly, the functional consequence of the spectrum of missense variants found across SKIC genes will be critical to understand the full translational potential of inhibiting the PELO–HBS1L rescue complex.

Here we describe a synthetic lethal interaction between two protein complexes which results in destabilization of the SKIC by mutually exclusive genetic events. Identification of further potential synthetic lethal interactions between tractable therapeutic targets and loss of a phenotypic complex will require expansion of the collaborative tools used here. Although large consortium efforts have characterized transcriptomes, genomes and dependencies of thousands of cancer cell models, the field remains limited by the number of cancer cell lines from which proteomic data have been generated. Improvement of the predictive power of dependencies and protein levels is dependent on

availability of whole-proteome data characterization across all cancer cell line models. The discovery of synthetic lethal relationships such as the one between PELO–HBS1L and SKIC will benefit from recent technical advancements, which are increasing the speed and sensitivity of data acquisition while reducing costs.

Online content

Any methods, additional references, Nature Portfolio reporting summaries, source data, extended data, supplementary information, acknowledgements, peer review information; details of author contributions and competing interests; and statements of data and code availability are available at <https://doi.org/10.1038/s41586-024-08398-6>.

- O’Neil, N. J., Bailey, M. L. & Hieter, P. Synthetic lethality and cancer. *Nat. Rev. Genet.* **18**, 613–623 (2017).
- Robson, M. et al. Olaparib for metastatic breast cancer in patients with a germline *BRCA* mutation. *N. Engl. J. Med.* **377**, 523–533 (2017).
- Chan, E. M. et al. WRN helicase is a synthetic lethal target in microsatellite unstable cancers. *Nature* **568**, 551–556 (2019).
- Lim, K. S. et al. USP1 is required for replication fork protection in *BRCA1*-deficient tumors. *Mol. Cell* **72**, 925–941.e4 (2018).
- Gallo, D. et al. CCNE1 amplification is synthetic lethal with PKMYT1 kinase inhibition. *Nature* **604**, 749–756 (2022).
- Zatreanu, D. et al. Polθ inhibitors elicit *BRCA*-gene synthetic lethality and target PARP inhibitor resistance. *Nat. Commun.* **12**, 3636 (2021).
- Kryukov, G. V. et al. *MTAP* deletion confers enhanced dependency on the PRMT5 arginine methyltransferase in cancer cells. *Science* **351**, 1214–1218 (2016).
- Tsherniak, A. et al. Defining a cancer dependency map. *Cell* **170**, 564–576.e16 (2017).
- Barretina, J. et al. The Cancer Cell Line Encyclopedia enables predictive modeling of anticancer drug sensitivity. *Nature* **483**, 603–607 (2012).
- Ghandi, M. et al. Next-generation characterization of the Cancer Cell Line Encyclopedia. *Nature* **569**, 503–508 (2018).
- Shi, X. et al. Building a translational cancer dependency map for The Cancer Genome Atlas. *Nat. Cancer* **5**, 1176–1194 (2024).
- Lelij, et al. Synthetic lethality between the cohesin subunits STAG1 and STAG2 in diverse cancer contexts. *eLife* **6**, e26980 (2017).
- Cairns, P. et al. Frequency of homozygous deletion at *p16/CDKN2* in primary human tumours. *Nat. Genet.* **11**, 210–212 (1995).
- Ikeuchi, K., Yazaki, E., Kudo, K. & Inada, T. Conserved functions of human Pelota in mRNA quality control of nonstop mRNA. *FEBS Lett.* **590**, 3254–3263 (2016).
- Shoemaker, C. J., Eyler, D. E. & Green, R. Dom34:Hbs1 promotes subunit dissociation and peptidyl-tRNA drop-off to initiate no-go decay. *Science* **330**, 369–372 (2010).
- Lee, H. H. et al. Structural and functional insights into Dom34, a key component of no-go mRNA decay. *Mol. Cell* **27**, 938–950 (2007).
- Navickas, A. et al. No-go decay mRNA cleavage in the ribosome exit tunnel produces 5’-OH ends phosphorylated by Trl1. *Nat. Commun.* **11**, 122 (2020).
- Arribere, J. A. & Fire, A. Z. Nonsense mRNA suppression via nonstop decay. *eLife* **7**, e33292 (2018).
- Green, R. & Guydosh, N. mRNA surveillance is driven by translation. *FASEB J.* **27**, 325.3–325.3 (2013).
- Tuck, A. C. et al. Mammalian RNA decay pathways are highly specialized and widely linked to translation. *Mol. Cell* **77**, 1222–1236.e13 (2020).
- Becker, T. et al. Structural basis of highly conserved ribosome recycling in eukaryotes and archaea. *Nature* **482**, 501–506 (2012).
- Pisareva, V. P., Skabkin, M. A., Hellen, C. U. T., Pestova, T. V. & Pisarev, A. V. Dissociation by Pelota, Hbs1 and ABCE1 of mammalian vacant 80S ribosomes and stalled elongation complexes. *EMBO J.* **30**, 1804–1817 (2011).
- DepMap, Broad. DepMap 23Q4 Public. *Figshare* <https://doi.org/10.25452/figshare.plus.24667905.v2> (2023).
- Aleksander, S. A. et al. The Gene Ontology knowledgebase in 2023. *Genetics* **224**, iyad031 (2023).
- Ashburner, M. et al. Gene Ontology: tool for the unification of biology. *Nat. Genet.* **25**, 25–29 (2000).
- Consortium, T. U. et al. UniProt: the universal protein knowledgebase in 2021. *Nucleic Acids Res.* **49**, D480–D489 (2020).
- Krepisch, A. C. et al. Germline DNA copy number variation in familial and early-onset breast cancer. *Breast Cancer Res.* **14**, R24 (2012).
- Weren, R. D. et al. Germline deletions in the tumour suppressor gene *FOCAD* are associated with polyposis and colorectal cancer development. *J. Pathol.* **236**, 155–164 (2015).
- Powers, K. T., Szeto, J.-Y. A. & Schaffitzel, C. New insights into no-go, non-stop and nonsense-mediated mRNA decay complexes. *Curr. Opin. Struct. Biol.* **65**, 110–118 (2020).
- Zinoviev, A., Ayupov, R. K., Abaeva, I. S., Hellen, C. U. T. & Pestova, T. V. Extraction of mRNA from stalled ribosomes by the Ski complex. *Mol. Cell* **77**, 1340–1349.e6 (2020).
- Traspas, R. M. et al. Loss of *FOCAD*, operating via the SKI messenger RNA surveillance pathway, causes a pediatric syndrome with liver cirrhosis. *Nat. Genet.* **54**, 1214–1226 (2022).
- Liu, X. et al. The PAF1 complex promotes 3’ processing of pervasive transcripts. *Cell Rep.* **38**, 110519 (2021).
- Nabet, B. et al. The dTAG system for immediate and target-specific protein degradation. *Nat. Chem. Biol.* **14**, 431–441 (2018).

34. Yagita, Y., Zavodszky, E., Peak-Chew, S.-Y. & Hegde, R. S. Mechanism of orphan subunit recognition during assembly quality control. *Cell* **186**, 3443–3459.e24 (2023).
35. Ohnuma, K. et al. Ski3/TTC37 deficiency associated with trichohepatoenteric syndrome causes mitochondrial dysfunction in *Drosophila*. *FEBS Lett.* **594**, 2168–2181 (2020).
36. Fabre, A. et al. SKIV2L mutations cause syndromic diarrhea, or trichohepatoenteric syndrome. *Am. J. Hum. Genet.* **90**, 689–692 (2012).
37. Bourgeois, P. et al. Tricho-hepato-enteric syndrome mutation update: mutations spectrum of TTC37 and SKIV2L, clinical analysis and future prospects. *Hum. Mutat.* **39**, 774–789 (2018).
38. Bonneville, R. et al. Landscape of microsatellite instability across 39 cancer types. *JCO Precis. Oncol.* <https://doi.org/10.1200/PO.17.00073> (2017).
39. Nusinow, D. P. et al. Quantitative proteomics of the Cancer Cell Line Encyclopedia. *Cell* **180**, 387–402.e16 (2020).
40. Picco, G. et al. Werner helicase is a synthetic-lethal vulnerability in mismatch repair-deficient colorectal cancer refractory to targeted therapies, chemotherapy, and immunotherapy. *Cancer Discov.* **11**, 1923–1937 (2020).
41. Guydosh, N. R., Kimmig, P., Walter, P. & Green, R. Regulated Ire1-dependent mRNA decay requires no-go mRNA degradation to maintain endoplasmic reticulum homeostasis in *S. pombe*. *eLife* **6**, e29216 (2017).
42. Wu, I.-H. et al. A role for the ribosome-associated complex in activation of the IRE1 branch of UPR. *Cell Rep.* **35**, 109217 (2021).
43. Zhou, J. et al. The crystal structure of human IRE1 luminal domain reveals a conserved dimerization interface required for activation of the unfolded protein response. *Proc. Natl Acad. Sci. USA* **103**, 14343–14348 (2006).
44. Hilal, T. et al. Structural insights into ribosomal rescue by Dom34 and Hbs1 at near-atomic resolution. *Nat. Commun.* **7**, 13521 (2016).
45. Shao, S. et al. Decoding mammalian ribosome-mRNA states by translational GTPase complexes. *Cell* **167**, 1229–1240.e15 (2016).
46. Terrey, M., Adamson, S. I., Chuang, J. H. & Ackerman, S. L. Defects in translation-dependent quality control pathways lead to convergent molecular and neurodevelopmental pathology. *eLife* **10**, e66904 (2021).
47. O'Connell, A. E. et al. Mammalian Hbs1L deficiency causes congenital anomalies and developmental delay associated with Pelota depletion and 80S monosome accumulation. *PLoS Genet.* **15**, e1007917 (2019).

Publisher's note Springer Nature remains neutral with regard to jurisdictional claims in published maps and institutional affiliations.



Open Access This article is licensed under a Creative Commons Attribution-NonCommercial-NoDerivatives 4.0 International License, which permits any non-commercial use, sharing, distribution and reproduction in any medium or format, as long as you give appropriate credit to the original author(s) and the source, provide a link to the Creative Commons licence, and indicate if you modified the licensed material. You do not have permission under this licence to share adapted material derived from this article or parts of it. The images or other third party material in this article are included in the article's Creative Commons licence, unless indicated otherwise in a credit line to the material. If material is not included in the article's Creative Commons licence and your intended use is not permitted by statutory regulation or exceeds the permitted use, you will need to obtain permission directly from the copyright holder. To view a copy of this licence, visit <http://creativecommons.org/licenses/by-nc-nd/4.0/>.

© The Author(s) 2025

Methods

Cell Lines

MDA-MB-231, NCI-H1299, PC-3, MCF7, HCC38, UMUC3, NCI-H1975, PANC-1, NCI-H460, MDA-MB-468, A549, NCI-H1437, SNU-449⁴⁸, U118-MG, CAPAN-1, DAOY, MIAPACA2, NCI-H838, NCI-H1755, LN18, NCI-H747, SW-837, T84, COLO205, COLO201, RKO, DLD-1, SW48, HEMa, TFF-1, ARPE-19, MCF-10A and HEK-293 cells were purchased from the American Type Culture Collection (ATCC). KYSE-450, MFE-319 and COLO678 cells were purchased from Leibniz Institute DSMZ. U87-MG was acquired from Ludwig Institute. LK-2 was acquired from the Japanese Collection of Research Biosources (JCRB), HT-29 was acquired from the National Institute of Health (NIH) and NCI-H322, HT115 and HT55 were acquired from the European Collection of Authenticated Cell Cultures (ECACC). All cell lines were confirmed for identity by short tandem repeat profiling and confirmed to be negative for mycoplasma. All cell lines were cultured in DMEM or RPMI (Gibco) supplemented with 10% heat inactivated FBS (Gibco).

Antibodies

The following primary antibodies were used to detect protein abundance in Simple Western assays: PELO (ProteinTech, 10582-1-AP), HBS1L (ProteinTech, 10359-1-AP), SKIV2L (ProteinTech, 11462-1-AP), TTC37 (Abcam, ab122421), WDR61 (Invitrogen, PA5-59052), FOCAD (Invitrogen, PA5-63051), AVEN (ProSci, 2413), ABCE1 (Abcam, ab185548), JNK (Cell Signaling, 4672), pJNK (Cell Signaling, 4668), p38 (Cell Signaling, 9212), phospho-p38 (Cell Signaling, 9211), EIF2S1 (Cell Signaling, 5324), phospho-EIF2S1 (Abcam, ab32157), IRE1α (Cell Signaling, 3294), pIRE1α (Novus Biologicals, NB100-2323), PERK (Cell Signaling, 3192), phospho-PERK (Cell Signaling, 3179), CHOP (ThermoFisher Scientific, MA1-250), JUN (Cell Signaling, 9165), p21 (Cell Signaling, 2947), PARP (Cell Signaling, 3898), HSP90 (Cell Signaling, 4877), GAPDH (Cell Signaling, 2118), HiBIT (Promega, N7200). Antibodies were diluted at 1:100 except for HSP90 (1:500) and GAPDH (1:3,000). High-content antibodies as follows: rabbit anti-IRE1α (Invitrogen PA5-20189), dilution 1:500. Goat anti-Rabbit IgG (H+L) Cross-Adsorbed Secondary Antibody, Alexa Fluor 568 (ThermoFisher A-11011), dilution 1:500.

In vivo studies

All animal studies were conducted in compliance with AbbVie's Institutional Animal Care and Use Committee and the National Institutes of Health Guide for Care and Use of Laboratory Animals guidelines in a facility accredited by the Association for the Assessment and Accreditation of Laboratory Animal Care.

In vivo CRISPR screening

MDA-MB-231 and NCI-H1299 cells were engineered to express enhanced Cas12a (enCas12a)⁴⁹, as described⁵⁰. Each line was transduced for 24 h with a Cas12a customized sgRNA library, as described¹¹ at a MOI of 0.3, maintaining continuous 1,000× coverage (3,000,000 cells per replicate) through selection. Following selection with 2 μg ml⁻¹ puromycin for 48 h, cells were washed briefly in media absent of antibiotics and inoculated into one flank (NCI-H1299) or into the mammary fat pad (MDA-MB-231) of 10 NOD scid gamma (NSG) mice per arm. Tumours were collected when measured at above 500 mm³ by calliper. DNA extraction, PCR and next-generation sequencing were performed as previously described⁵¹ at 1,000× coverage using 120-nt single-end reads on a NextSeq 500 (Illumina). All cells and lentivirus used were tested for rodent pathogens and mycoplasma by IDEXX Bioanalytics.

CRISPR and siRNA validation of PELO and HBS1L dependency

For CRISPR–Cas9 knockout, unless otherwise noted, negative control guides were targeted to the non-essential gene *B2M*. Positive control guides include those designed to target essential genes (*RAN* and *RPA3*) and the common essential gene (*ABCE1*). A full list of sgRNA sequences

used can be found in Supplementary Table 1. To perform CRISPR gene editing across cancer cell lines, we utilized electroporation of ribonucleoprotein complexes (RNPs). In short, functional sgRNA duplexes were created by hybridizing Alt-R CRISPR–Cas9 CRISPR RNA (IDT) with Alt-R CRISPR–Cas9 *trans*-activating CRISPR RNA (IDT). These sgRNA complexes were incubated with Alt-R *Streptococcus pyogenes* Cas9 Nuclease V3 (IDT) and electroporation enhancer (IDT) to create RNPs, which were then electroporated into the cell using the Invitrogen's Neon NxT Electroporation system according to the manufacturer's protocol.

To generate doxycycline-inducible models, MIAPACA2 cells were stably derived via lentiviral infection of pXPR_BRD101⁵² (Broad Institute). After Cas9 infection and selection with 20 μg ml⁻¹ blasticidin (Gibco), Cas9 activity was measured and deemed sufficient if at least 80% knockout of a known control gene was achieved. All Cas9 models described in this study are polyclonal unless otherwise mentioned. After confirmation of Cas9 activity, doxycycline-inducible NTC, *PELO* or *HBS1L* sgRNA constructs (Celllecta) were stably integrated by 2 μg ml⁻¹ puromycin selection. Generated doxycycline-inducible Cas9–sgRNA cells were cultured in RPMI supplemented with 10% tetracycline (tet) free FBS (Takara), treated with 2 μg ml⁻¹ doxycycline (Sigma) to induce knockout and validated by western blot.

For small interfering RNA (siRNA) validation of HAP1 (Horizon Discovery) dependency, cells with or without *SKIV2L* knockout were plated at 1,000 cells per well in 96-well plates and reverse transfected with 10 nM NTC (Dharmacon, J-008702-06), *PELO* (Dharmacon, J-019068-11) or *ABCE1* (Dharmacon, J-008702-06) siRNAs and Lipofectamine RNAiMAX (Invitrogen) according to manufacturer's protocol. Knockdown efficiency was measured by Simple Western at 48 h post transfection. ON-Targetplus Non-targeting siRNA (D-001810-01-20): UGGUUUAC AUGUCGACUAA; ON-Targetplus Human *PELO* siRNA (J-019068-11): GUGUGGUACUGGAGCGCAU; ON-Targetplus Human *ABCE1* siRNA (J-008702-06): UGUCUCAGCUUGAAAUUAC.

Cell proliferation assays

Cells were plated at 1,000 cells per well (unless otherwise noted) in 96-well plates (Corning, 3903). Cell viability was assessed on day seven unless otherwise noted using CellTiter-Glo 2.0 Cell Viability Assay, according to manufacturer's protocol (Promega, G9241), and luminescence was quantified using a PerkinElmer Envision (2104 Multilabel Reader). Cell confluency was assessed continually through Incucyte (Satorius v2022B).

Gene dependency data and informatic correlations

CRISPR dependency data can be located via the 23Q4 DepMap Public database. Two-group and continuous Pearson's correlations of PELO CRISPR dependency data to other features were taken from the 23Q4 DepMap public portal using either mRNA expression and/or proteomic data taken from CCLE cohorts as of the 23Q4 DepMap Public release. Gene dependency, RNA, and proteomic data can be downloaded at <https://depmap.org>.

Conditional in vivo knockout studies

For these studies, female CB17.SCID (Charles River Laboratories) mice were used. To generate xenografts from MIAPACA2-Cas9 doxycycline-sgNTC, sgPELO or sgHBS1L cells, mice were inoculated subcutaneously into the right hind flank with 5 × 10⁶ viable cells. The injection volume was 0.1 ml and composed of a 1:1 mixture with Matrigel (BD). Measurements of the length (*L*) and width (*W*) of the tumour were taken via electronic calliper twice weekly and the tumour volume was calculated according to the following equation: volume = $L \times W^2/2$. Mice were assigned to 2 treatment groups of 8 mice each so that the mean tumour volumes within groups were approximately 175–250 mm³. Groups were then assigned to a diet of regular chow or doxycycline chow containing 625 mg of doxycycline per kg of chow (TD.01306 Rodent Diet, Teklad). Mice were euthanized: (1) when tumour volume reached

2,000 mm³; (2) when general efficacy parameters were confidently determined; or (3) when other animal health issues were observed.

Additional cohorts of mice were entered into a biomarker study, to determine the effect of doxycycline induction on PELO and HBS1L expression in the appropriate tumour constructs. After staging into groups of 4 mice each and given access to regular chow or to doxycycline chow, tumours were excised from mice and snap frozen after 8 days, 14 days, and 21 days and analysed by Simple Western.

Exogenous expression constructs

Protein-coding expression sequences were cloned into a version of pGenLenti (lentiviral construct; Genscript) that was modified to replace the *IRES* sequence with an SV40 promoter to drive expression of the puromycin resistance cassette. The full-length wild type was generated from NM_015946.5 (*PELO* open reading frame (ORF)), NM_006620.4 (*HBS1L* ORF, isoform 1) or NM_006929.5 (*SKIV2L* ORF) and truncated fragments were synthesized and inserted using the *NheI*–*NotI* sites. All point mutants were generated using site directed mutagenesis. Sequences for the final vectors with inserts are listed in Supplementary Table 7.

Determination of protein abundance by Simple Western

Protein was extracted in CellLytic M lysis buffer (Sigma) containing cOmplete protease, phosSTOP phosphatase inhibitors (Roche), Benzonase (Sigma) and 1 mM dithiothreitol (Sigma). Sample protein concentration was measured using Pierce BCA Protein Assay reagent (ThermoFisher Scientific) and diluted to 0.5 µg µl⁻¹ for analysis using Simple Western Jess System (Bio-Techne). Simple Western was performed according to the manufacturer's protocol, and results were analysed using Compass software (version 6.2.0).

Isogenic model development and validation

Isogenic NCI-H1299 cell models with *PELO*, *HBS1L*, *SKIV2L*, *TTC37*, *FOCAD* or *AVEN* clonal knockout were generated via electroporation of RNPs targeting the indicated genes of interest or a negative control (*B2M*). To attain clonal populations, these bulk populations were then seeded in 96-well plates at a concentration of 0.25 cells per well. After 3–4 weeks, wells containing a single colony were picked and expanded. Individual clones were verified for complete knockout by Simple Western.

PELO SL-ID CRISPR screen and analysis

A library was designed for spCas9 containing 7,092 sgRNAs with 4 sgRNA constructs per gene. The lentiviral CRISPR library was produced in HEK293T cells following CRISPR & Mission Lentiviral packaging mix protocol (Sigma) and concentrated 1:10 using Lenti-X concentrator (Takara). NCI-H1299 cells engineered to express spCas9 were transduced with titrated lentiviral guide library to ensure low MOI. Cells were seeded with 5 million cells in T175 plates and infected at an MOI of approximately 0.3 at 500× representation using 5 µg ml⁻¹ polybrene. After infection and 48 h of selection with 2 µg ml⁻¹ puromycin, cells were either collected to assess basal library representation or maintained at 500× library representation for 14 days to allow for guide dropout and enrichment. gDNA was isolated using Nucleospin Blood kit (Takara) by manufacturer guidelines. Library generation, sequencing, and analysis of the screen were carried out as previously described⁵¹.

RNA quantification

MIAPACA2 FOCAD-dTAG cells were plated at 1 × 10⁶ per 100 mm cell culture dish for RNA extraction. Cells were treated with 500 nM dTAGV-1 (HY-145514C, MedChemExpress) or DMSO, and samples were collected at indicated timepoints. Cells for total RNA collection were lysed on plate using RLT buffer and homogenized using QIAshredder (Qiagen) before being purified using RNeasy RNA purification kit (Qiagen) per manufacturer guidelines. Pellets for Simple Western were processed and analysed as previously described.

RNA concentration was measured by NanoVue Plus Spectrophotometer and cDNA was generated using 1 µg RNA with Superscript Vilo Master Mix (ThermoFisher Scientific) per manufacturer guidelines. Complementary DNA (cDNA) was diluted 1:100 in DEPC-treated water and two-step quantitative PCR with reverse transcription was performed in triplicate in a MicroAmp Optical 384-well reaction plate (ThermoFisher Scientific) using 3 µl diluted cDNA, 6 µl 1× Power Sybr Green PCR Master mix (ThermoFisher Scientific), 3 µl 1 µM RxNReady Primer Pools (IDT) for either *FOCAD*, *SKIV2L*, *TTC37*, *AVEN* or *GAPDH*, and 8 µl water. Samples were amplified using QuantStudio 6 Flex (ThermoFisher Scientific) and analysed with QuantStudio Real-Time PCR System software (version 1.3) following manufacturer guidelines. Relative quantification of gene expression was carried out with the $\Delta\Delta C_t$ method using housekeeping gene *GAPDH* C_t values and matching DMSO controls. Primers used for transcript analysis are as follows: *FOCAD*: ATGAAGC CAGCCTCTCCTCAGA, CTGGGTTGGTATGGCTATCCAC; *SKIV2L*: GCC CAGAAACACATGACTCG, CGAAGGATCTCCGTGGTC; *TTC37*: TCCAGGT GATCCTGCTATCT, CTATCCTCTTTGGCTGAGTGTT; *AVEN*: GTCTCAGG ACCTGAAATCCAAGG, GGAGGTAAGTGGTTGCTCAGGT; and *GAPDH*: GTCTCCTCTGACTTCAACAGCG, ACCACCCTGTTGCTGTAGCCAA.

High-content analysis

Cells were washed with PBS followed by a 10-min incubation with 0.25% Triton X-100 in PBS. Plates were washed and incubated for 30 min in Click-iT EdU cocktail (Thermo C10640) followed by a second wash. Blocking solution consisting of 1% BSA in PBS was added to the plates and incubated for 30 min followed by wash. Hoechst 33342 was diluted 1:1,000 in 0.6% BSA in PBS and incubated for 30 min on plates, which were then washed and left in PBS. Plates were scanned on Thermo CX7 LZR using filter sets 405LZR_BGRFR_BGRFR (nuclei) and 647LZR_BGRFR_BGRFR (Edu). Nuclei were identified and Edu quantified using HCS Studio Target Activation.V4 algorithm.

For IRE1α foci quantification, cells were washed with PBS followed by a 15-min incubation with blocking buffer (1% BSA, 0.25% Triton X-100, 10% goat serum in PBS). Plates were washed and incubated with 1:500 diluted rabbit anti-IRE1α polyclonal antibody (Invitrogen PA5-20189) in blocking buffer at 4 °C overnight. The plates were washed and incubated with 1:500 Goat anti-Rabbit IgG (H+L) Cross-Adsorbed Secondary Antibody, Alexa Fluor 568 (ThermoFisher A-11011) and 1:1,000 Hoechst 33342 diluted in 1% BSA in PBS for 60 min, washed and left in PBS. Plates were scanned on Thermo CX7 LZR using filter sets 405LZR_BGRFR_BGRFR (nuclei) and 561LZR_BGRFR_BGRFR (IRE1α). Nuclei were identified and IRE1α quantified using HCS Studio Target Activation.V4 algorithm.

Cell cycle and death analysis

For flow cytometry-based methods, cells were prepared for cell cycle analysis using the Click-iT EdU Alexa Fluor 647 Flow Cytometry Assay Kit (Invitrogen) according to the manufacturer's protocol. In brief, cells were cultured in EdU (10 µM) for 1.5–2 h prior to fixation, permeabilization, and incubation with the Click-iT reaction cocktail composed of PBS, CuSO₄, Alexa Fluor 647, and buffer additive. Cells were then washed 2 times with 1× Click-iT permeabilization/wash reagent and resuspended in 500 µl FxCycle PI/RNase staining solution (Invitrogen). Cells were incubated at 4 °C for at least 15 min prior to analysis.

Cells were prepared for viability analysis using Apotracker Green (BioLegend), MitoTracker Red CMXRos (Invitrogen), and Celcein Blue AM (Invitrogen) dyes according to the manufacturers' protocols. In brief, cells were collected, washed in FACS staining buffer (PBS + 1% BSA), and incubated in 400 nM Apotracker green for 20 min in the dark at room temperature. Cells were then washed in PBS and resuspended in 1 ml PBS containing 2 µl Calcein Blue (final concentration 1 µM) and 0.5 µl MitoTracker Red. Cells were incubated for 30 min at room temperature prior to analysis. All analyses were done on a Novo-Cyte Quanteon flow cytometer.

For Incucyte cell death assays, cells were electroporated to knock out the indicated genes and cultured in 96-well plates at 1,000 cells per 100 μ l per well for 24 h prior to addition of either Cytotox Red or Annexin V Green (Sartorius) dye. The Cytotox Red dye was diluted 1:2,000 in RPMI to generate a 500 nM solution; 100 μ l were added to each well for a final concentration of 250 nM Cytotox Red per well. The Annexin V Green dye was solubilized in 100 μ l PBS and diluted 1:100 in RPMI before adding 100 μ l to each well to generate a final dilution of 1:200. Cell growth and fluorescence were monitored over time using the Sartorius Adherent Cell-by-Cell Analysis Module.

Transcriptomic analysis

Total RNA was collected from cell pellets using RNeasy columns (Qiagen). Libraries were prepped using the NEB Ultra II RNA library prep kit and sequenced on NextSeq HighOutput 300-Cycle flow cell (2 \times 100bp). Data were analysed as follows. Reads were aligned using Illumina DRAGEN v4.0. Counts were calculated using featureCounts from subread package and subsequently adjusted with TMM normalization and limma-voom transformation. Differential expression analysis was performed using limma. Gene set enrichment analyses were performed using the fgsea package.

Molecular modelling of PELO–HBS1L complex

A model of the PELO–HBS1L interaction was generated by first extracting the 3D coordinates for gene PELO (chain HC, named by authors as IIJ) and for gene HBS1L (chain IC, named by authors as JJ) from the experimental ribosomal complex published under Protein Data Bank ID 5LZZ (electron microscopy). The electron microscopy structure displays every residue in the full-length PELO protein (1–385), but the first 259 residues of HBS1L are not resolved, displaying only residues 260–684 of the 684-amino acid HBS1L protein. Coordinates were then imported into the visualization program PyMol (version 1.7.6.6, Schrödinger). Protein backbone ribbon styling, background settings, key residue highlights (with stick) and sectional colouring were applied.

HBS1L immunoprecipitation

Cells were washed on ice in cold PBS and collected in cold IP lysis buffer (Pierce) supplemented with cOMplete mini EDTA free protease inhibitor and phosSTOP mini phosphatase inhibitor (Roche). Following lysis at 4 °C under constant agitation and centrifugation at 4 °C and 12,000 r.p.m., lysate concentration was quantified using Pierce BCA Protein Assay reagent (ThermoFisher Scientific). Lysate (1–2 mg) was incubated overnight under constant agitation at 4 °C with either HiBIT monoclonal (Promega) or mouse IgG antibody (Sigma-Aldrich); remaining lysate was reserved for input samples. The next morning, lysates were incubated with Dynabeads protein G (ThermoFisher Scientific) for 1 h under constant agitation at 4 °C and washed 3 times with IP lysis buffer. To elute, beads were incubated at 95 °C for 5 min in 1 \times Protein Simple master mix consisting of dithiothreitol, sample buffer and fluorescent master mix. Simple Western was performed according to

manufacturer's protocol, and results were analysed using Compass software (version 6.2.0).

Reporting summary

Further information on research design is available in the Nature Portfolio Reporting Summary linked to this article.

Data availability

Source images for Protein Simple protein blots are available in Supplementary Fig. 1. RNA-seq data are available through the Gene Expression Omnibus (GEO) under accession number GSE261804. Figs. 1a and 2c were created in BioRender.com (Plotnik, J. (2025) <https://biorender.com/s15m274> and <https://biorender.com/x63t552> (2025)). Tumour genomic data in this paper were generated by TCGA Research Network (<https://www.cancer.gov/tcga>) and accessible publicly at <https://cbioportal.org>. Tumour proteomic data used in this publication was generated by the National Cancer Institute CPTAC. Source data are provided with this paper.

48. Park, J. et al. Characterization of cell lines established from human hepatocellular carcinoma. *Int. J. Cancer* **62**, 276–282 (1995).
49. Kleinstiver, B. P. et al. Engineered CRISPR–Cas12a variants with increased activities and improved targeting ranges for gene, epigenetic and base editing. *Nat. Biotechnol.* **37**, 276–282 (2019).
50. DeWeirdt, P. C. et al. Optimization of AsCas12a for combinatorial genetic screens in human cells. *Nat. Biotechnol.* **39**, 94–104 (2021).
51. Petiwala, S. et al. Optimization of genomewide CRISPR screens using AsCas12a and multi-guide arrays. *CRISPR J.* **6**, 75–82 (2023).
52. Hong, A. L. et al. Integrated genetic and pharmacologic interrogation of rare cancers. *Nat. Commun.* **7**, 11987 (2016).

Acknowledgements Financial support for this research was provided by AbbVie. We thank all members of Oncology Discovery Research at AbbVie for productive conversations and feedback on this manuscript. AbbVie is an industry partner in the DepMap consortium (DMC) and Functional Genomics Consortium (FGC). The authors thank members and leadership of the Broad DepMap and Functional Genomics Consortia for their continued support and productive collaboration throughout consortium activities.

Author contributions V.P., A.E.R., K.R.S., S.K., K.K., D.C., D.W., P.L., S.P., M.T., A.C., S.W., M.B.P., D.M., V.M., X.S., C.L., S.S., Z.D., F.G.B., D.V., B.B., J.A.M., W.N.P. and J.P.P. contributed to the design of this study. V.P., A.E.R., K.R.S., K.K., P.L., S.P., M.B.P., D.M., V.M., S.S., D.V., B.B. and J.P.P. were involved in the generation of in vitro data. D.C., D.W., P.L., F.G.B. and J.A.M. were involved in the design and generation of in vivo studies. S.K., A.C., X.S., C.L. and Z.D. were responsible for informatic analyses. M.T. was responsible for molecular modelling and visualization data. V.P., A.E.R., K.R.S., S.K., M.B.P., W.N.P. and J.P.P. were responsible for figure generation, writing the manuscript and edits.

Competing interests V.P., A.E.R., K.S., S.K., K.K., D.C., D.W., P.L., S.P., M.T., A.C., S.W., M.B.P., D.M., V.M., X.S., C.L., S.S., Z.D., G.B., D.V., B.B., J.A.M., W.N.P. and J.P.P. are employees of AbbVie.

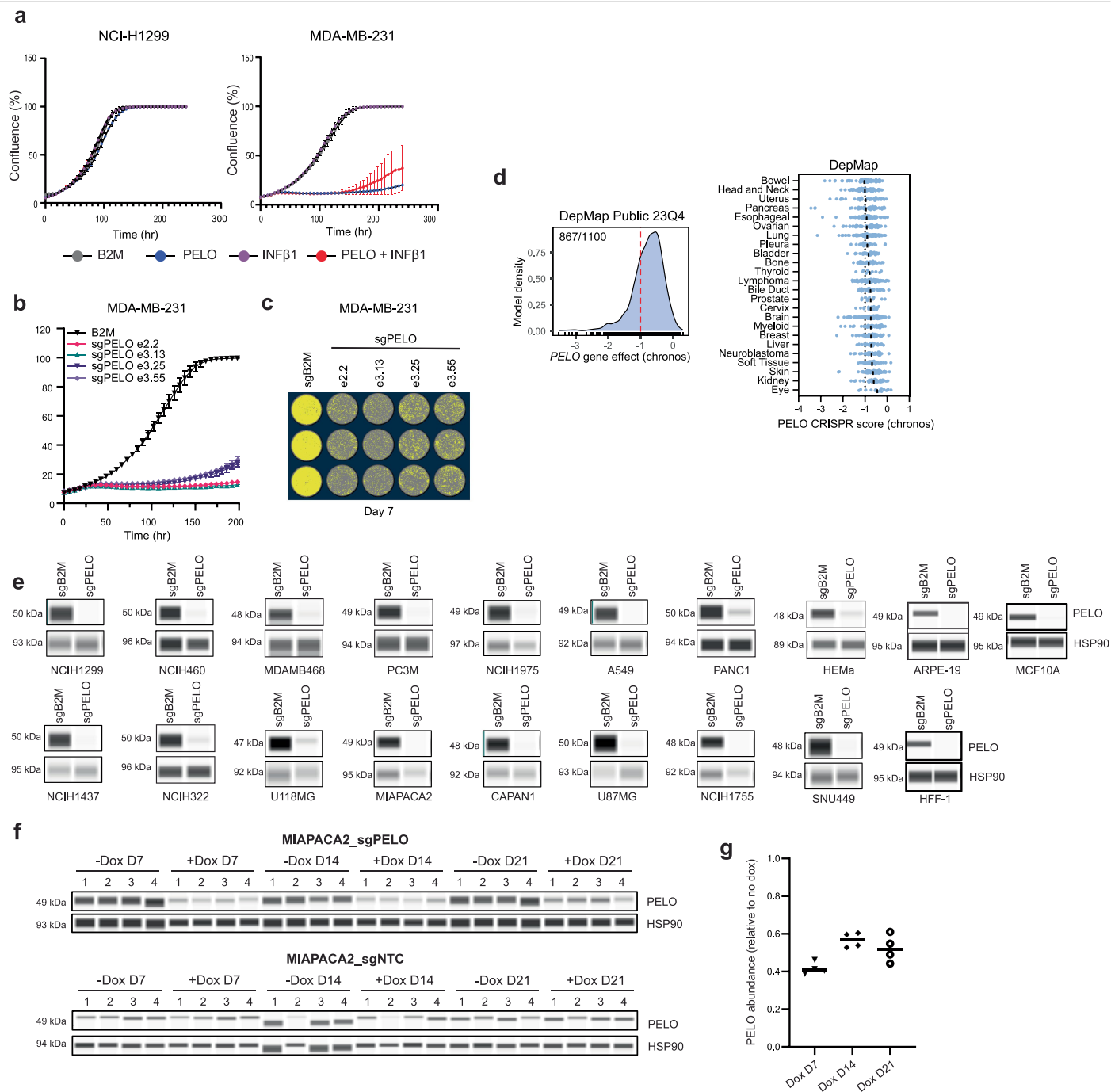
Additional information

Supplementary information The online version contains supplementary material available at <https://doi.org/10.1038/s41586-024-08398-6>.

Correspondence and requests for materials should be addressed to Joshua P. Plotnik.

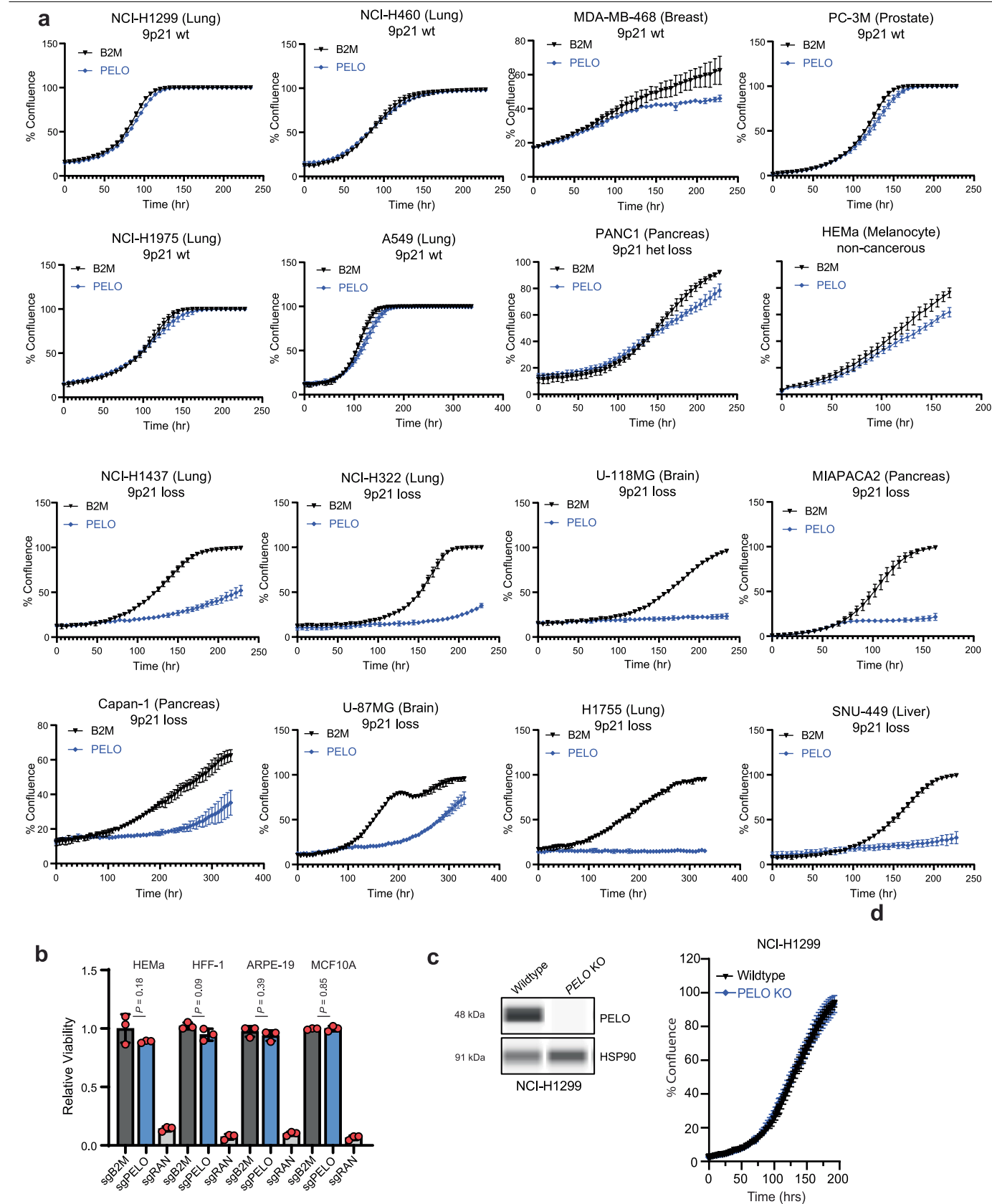
Peer review information Nature thanks Jeremy Setton and the other, anonymous, reviewer(s) for their contribution to the peer review of this work. Peer review reports are available.

Reprints and permissions information is available at <http://www.nature.com/reprints>.



Extended Data Fig. 1 | Validation of PELO dependency in vitro and in vivo. (a) in vitro validation of *IFNB1/PELO* in NCI-H1299 and MDA-MB-231. (b) Confluency MDA-MB-231 cells after transfection with sgB2M or four independent sgRNA's targeting *PELO* (e2.2, e3.13, e3.25, e3.55). (c) Image on day 7 of Incucyte experiment shown in (b); cells outlined in yellow to show confluence. (d) *PELO* gene effect density plot across all models available in DepMap Public release 23Q4 ($n = 1100$) and *PELO* Chronos scores across all major lineages available in DepMap Public release 23Q4. Red line delineates highly dependent models. (e) sgPELO knockout efficiency in models tested

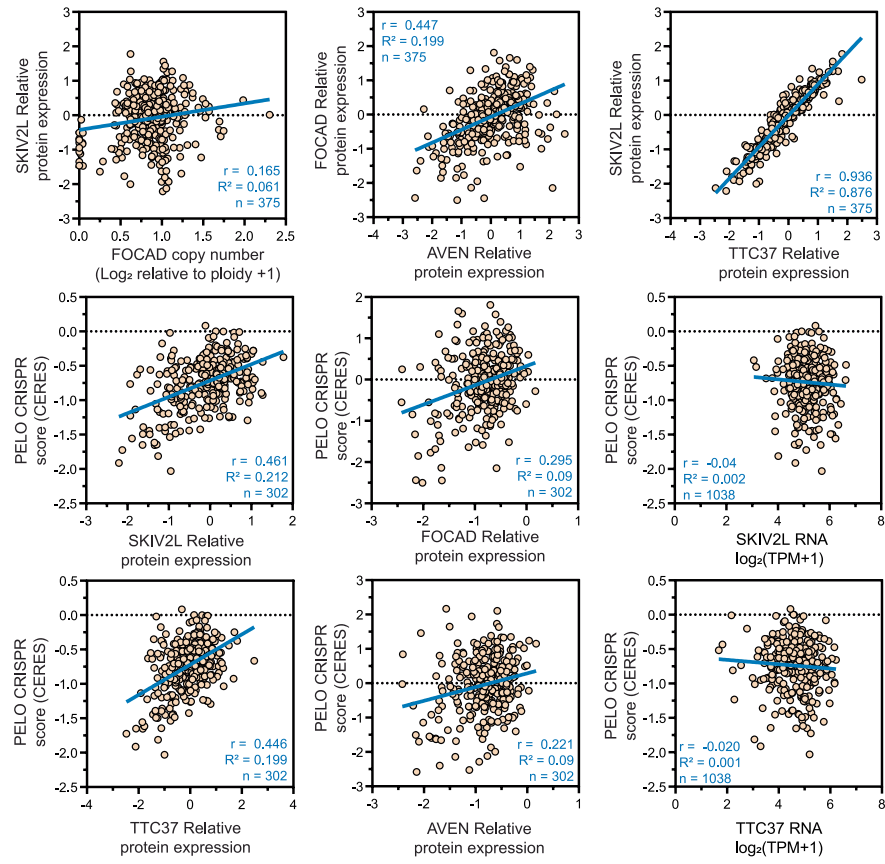
in Fig. 1g. Representative image of one experiment of two independent biological replicates shown. (f) Validation of PELO knockout in the MIAPACA-2 *in vivo* doxycycline inducible sgPELO or sgNTC study. Four independent tumors harvested at each time-point post dox (D7, D14, D21) for both the no dox and dox conditions. (g) Quantification of PELO protein levels from (f). Mean of $n = 4$ animals per group, relative to no dox control. Data (a, b) shown as mean \pm s.e.m. Data shown as $n = 3$ independent biological replicates (a, b), representative data shown from one of three independent replicates (c).



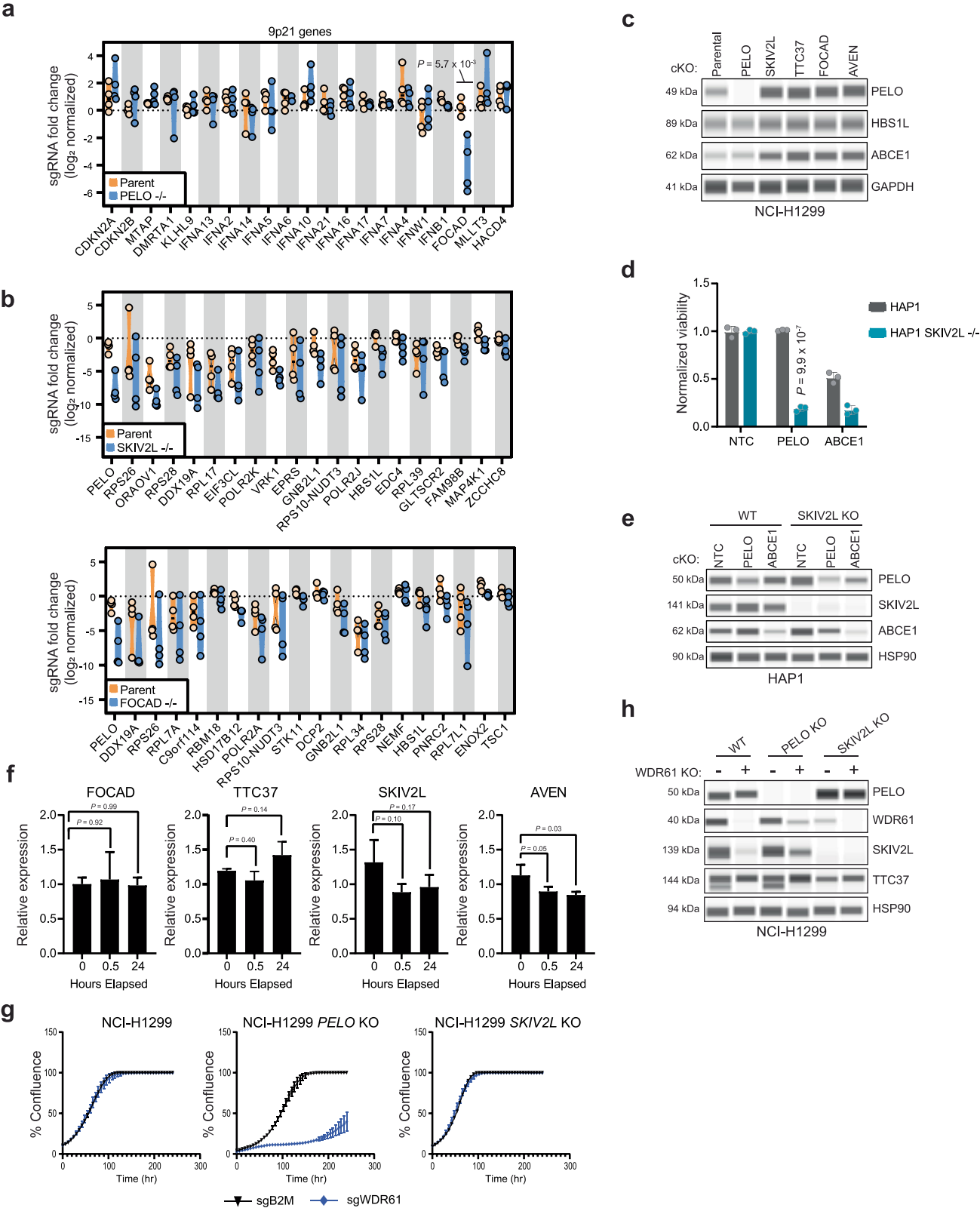
Extended Data Fig. 2 | In vitro growth curves after PELO knockout. (a) Growth of sgB2M (black) and sgPELO (blue) models reported in Fig. 1g. $n = 2$ independent biological experiments, shown as mean \pm s.e.m. (b) Effect of sgPELO on normal immortalized cell models, HEMa, $P = 0.18$; HFF-1, $P = 0.09$; ARPE-19, $P = 0.39$; MCF10A, $P = 0.85$. Negative control: B2M sgRNA. Pan essential control: RAN

sgRNA. Data shown as mean \pm s.e.m, $n = 3$ biologically independent replicates. (c) Stable NCI-H1299 sgPELO model generation verified by immunoblot and growth rate of NCI-H1299 wildtype as compared to sgPELO. Data shown as mean \pm s.e.m, $n = 2$ biologically independent experiments.

a



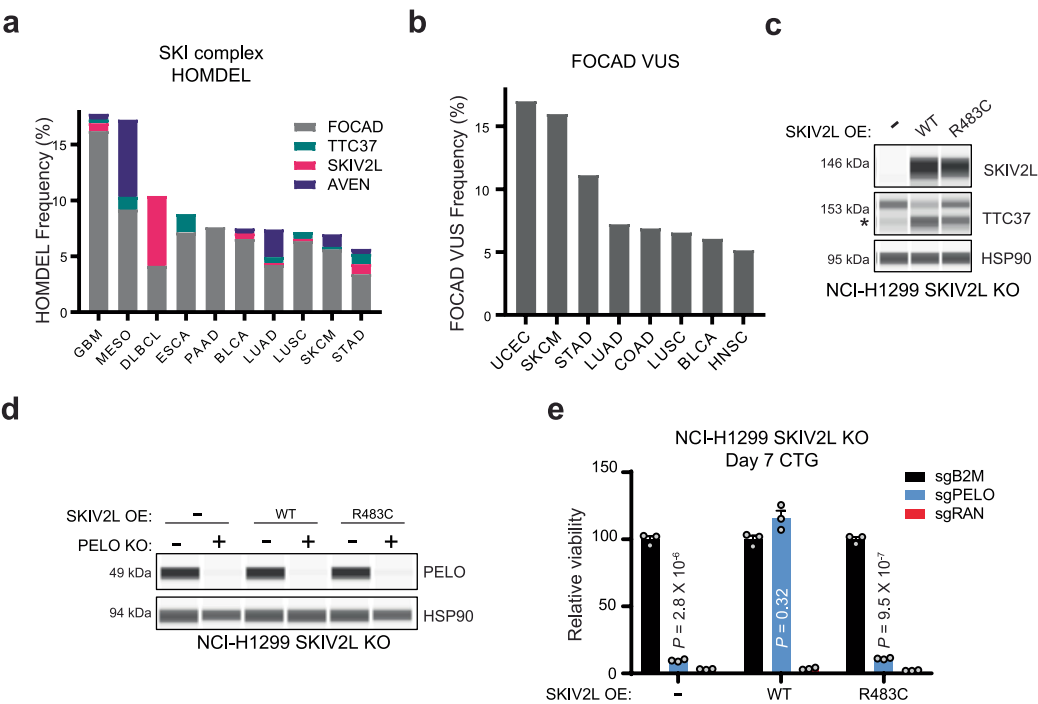
Extended Data Fig. 3 | Protein and mRNA correlations of SKIc members. (a) DepMap correlations of genomic and dependency features (protein, copy number, RNA expression) between SKIc members and *PELO* dependency. Pearson r calculated for each comparison.



Extended Data Fig. 4 | See next page for caption.

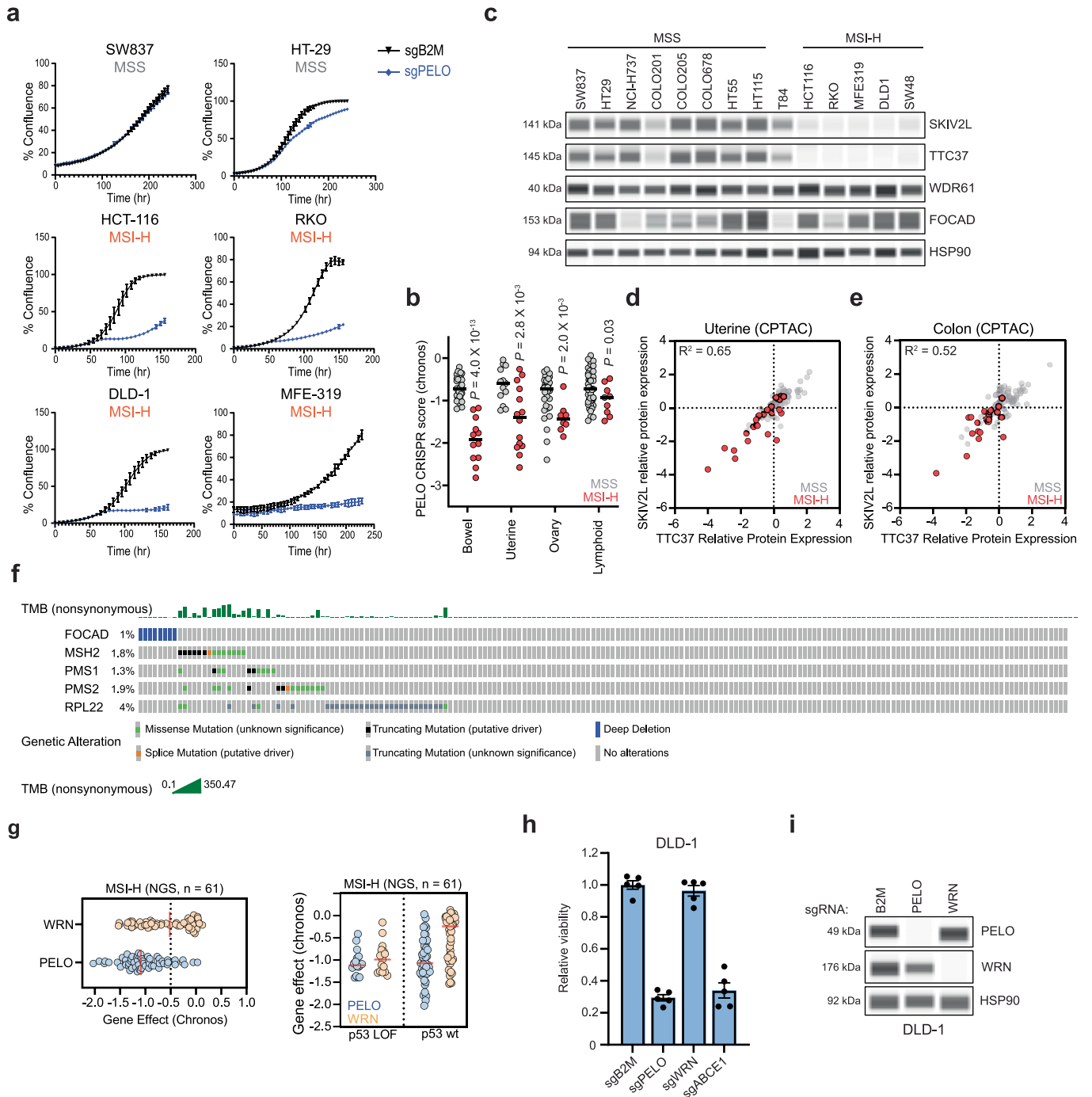
Extended Data Fig. 4 | Characterization of SKIc loss and relationship with PELO. (a) Guide level analysis of 9p21 genes. NCI-H1299 parent (orange) and *PELO*^{-/-} (blue) models shown. Two-tailed Student's *t*-test of $n = 4$ sgRNA per gene, Parent vs. *PELO*^{-/-}; FOCAD, $P = 5.7 \times 10^{-3}$. (b) SL-ID screen results in *SKIV2L*^{-/-} and *FOCAD*^{-/-} models. NCI-H1299 parental (orange) *SKIV2L*^{-/-} or *FOCAD*^{-/-} (blue). Each dot represents an individual sgRNA ($n = 4$) for each gene, mean of $n = 3$ independent biological replicates. (c) Immunoblot of the PELO/HBS1L/ABCE1 rescue complex across isogenic SKIc knockout models. (d) PELO dependency by siRNA in HAP1 or HAP1 *SKIV2L*^{-/-} models. Data shown as mean \pm s.e.m, $n = 3$ biologically independent replicates, two-tailed Student's

t-test; $P = 9.9 \times 10^{-7}$. (e) Validation of siRNA efficiency by immunoblot in (d). Data generated from a single experiment. (f) RNA quantification of SKIc levels (FOCAD, TTC37, SKIV2L, AVEN) post FOCAD degradation. Data shown as mean \pm s.e.m, $n = 3$ biologically independent replicates, two-tailed Student's *t*-test. (g) sgWDR61 in NCI-H1299 parental, *PELO*^{-/-}, and *SKIV2L*^{-/-} models. Confluency of sgB2M (black), sgWDR61 (blue). Data shown as mean \pm s.e.m, $n = 3$ biologically independent replicates (h) Immunoblot validation of sgWDR61 efficiency and effects on SKIc in models from (g). Data is generated from a single independent experiment.



Extended Data Fig. 5 | SKI complex perturbations in cancer. (a) Stacked bar chart of the frequency of homozygous deletions of *FOCAD* (grey), *TTC37* (teal), *SKIV2L* (fuchsia), *AVEN* (purple) across TCGA cohorts with prevalence greater >5%. (b) Frequency of *FOCAD* mutations occurring across TCGA cohorts with prevalence >5%. (c) Generation of a SKIV2L rescue model in the NCI-H1299 SKIV2L KO cell line; validation of SKIV2L and TTC37 expression. Data is a representative image of a single replicate of $n = 2$ independent biological experiments. (d) PELO knockout in the panel of SKIV2L KO, SKIV2L WT rescue

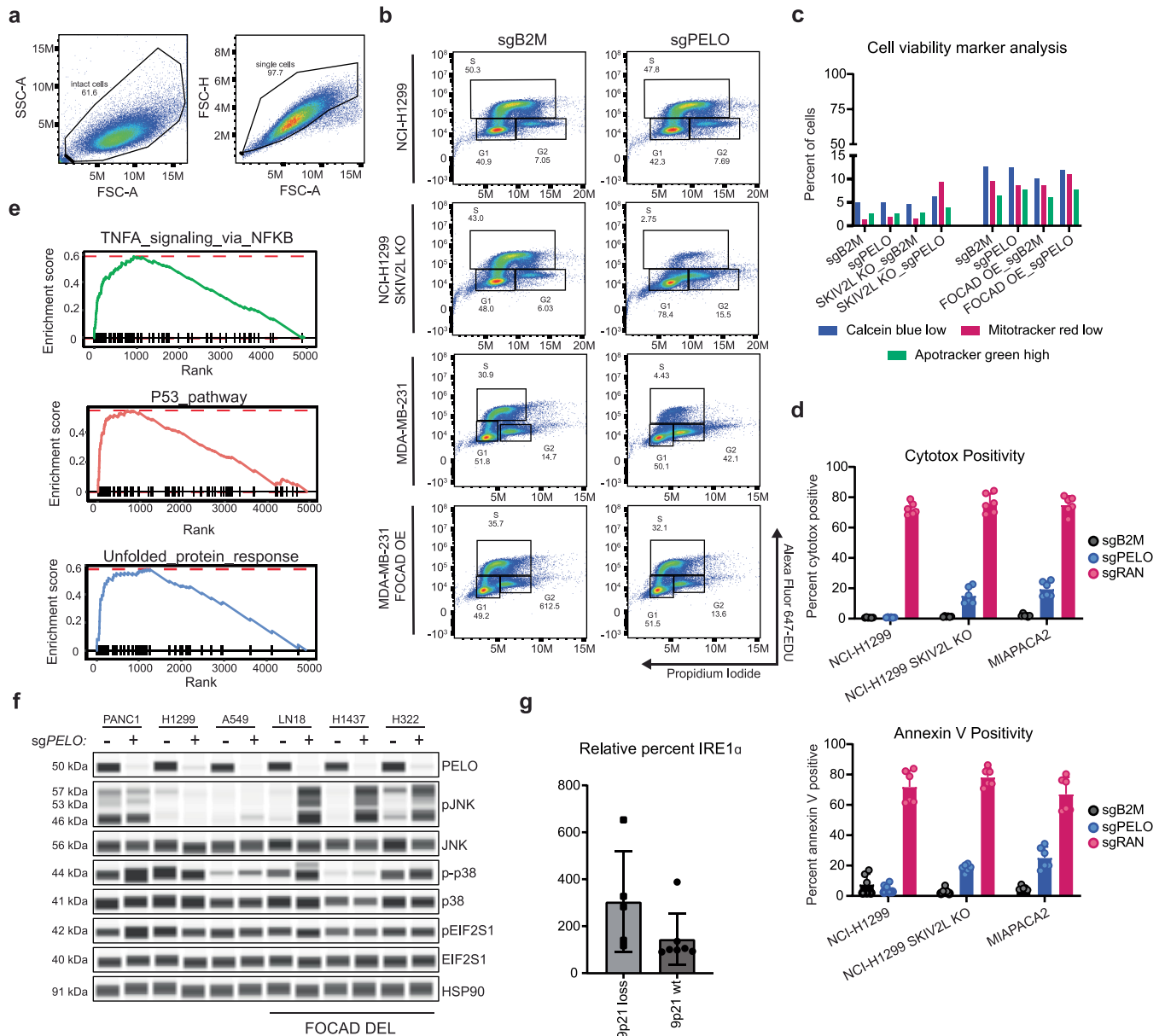
or SKIV2L R483C rescue cells. Data is a representative image of a single replicate of $n = 3$ independent biological experiments. (e) Relative viability of SKIV2L KO (–), SKIV2L WT rescue or SKIV2L R483C rescue cell lines measured 7 days after sgB2M (black), sgPELO (blue), or sgRAN (red) transfection. Data shown as mean \pm s.e.m., $n = 3$ biologically independent replicates, two-tailed Student's t -test between sgB2M and sgPELO groups; SKIV2L KO, $P = 2.8 \times 10^{-6}$; SKIV2L WT, $P = 0.32$; R483C, $P = 9.5 \times 10^{-7}$.



Extended Data Fig. 6 | SKIc and PELO synthetic lethality in MSI-H cancers.

(a) PELO is a selective dependency in MSI-H cell lines. A panel of MSS (SW837, HT-29) and MSI-H (HCT-116, RKO, DLD1, MFE-319) cell lines after sgB2M (black) or sgPELO (blue). Data shown as mean \pm s.e.m., $n = 3$ biologically independent replicates. (b) PELO DepMap Chronos dependency in MSI-H models as part of major MSI lineages. Models characterized by NGS MSI status, MSS (grey) or MSI-H (red). Two-tailed Student's t -test of MSI to MSS by lineage; Bowel, $P = 4.0 \times 10^{-13}$; Uterine, $P = 2.8 \times 10^{-3}$; Ovary, $P = 2.0 \times 10^{-3}$; Lymphoid, $P = 0.03$. (c) SKIc immunoblot in MSI and MSS models. Data is derived from one biological experiment. (d) Correlation of SKIV2L and TTC37 relative protein levels from uterine cancer CPTAC proteomic data ($n = 116$). MSI-H tumors highlighted in red. Pearson's coefficient of determination, $R^2 = 0.65$. (e) Correlation of SKIV2L

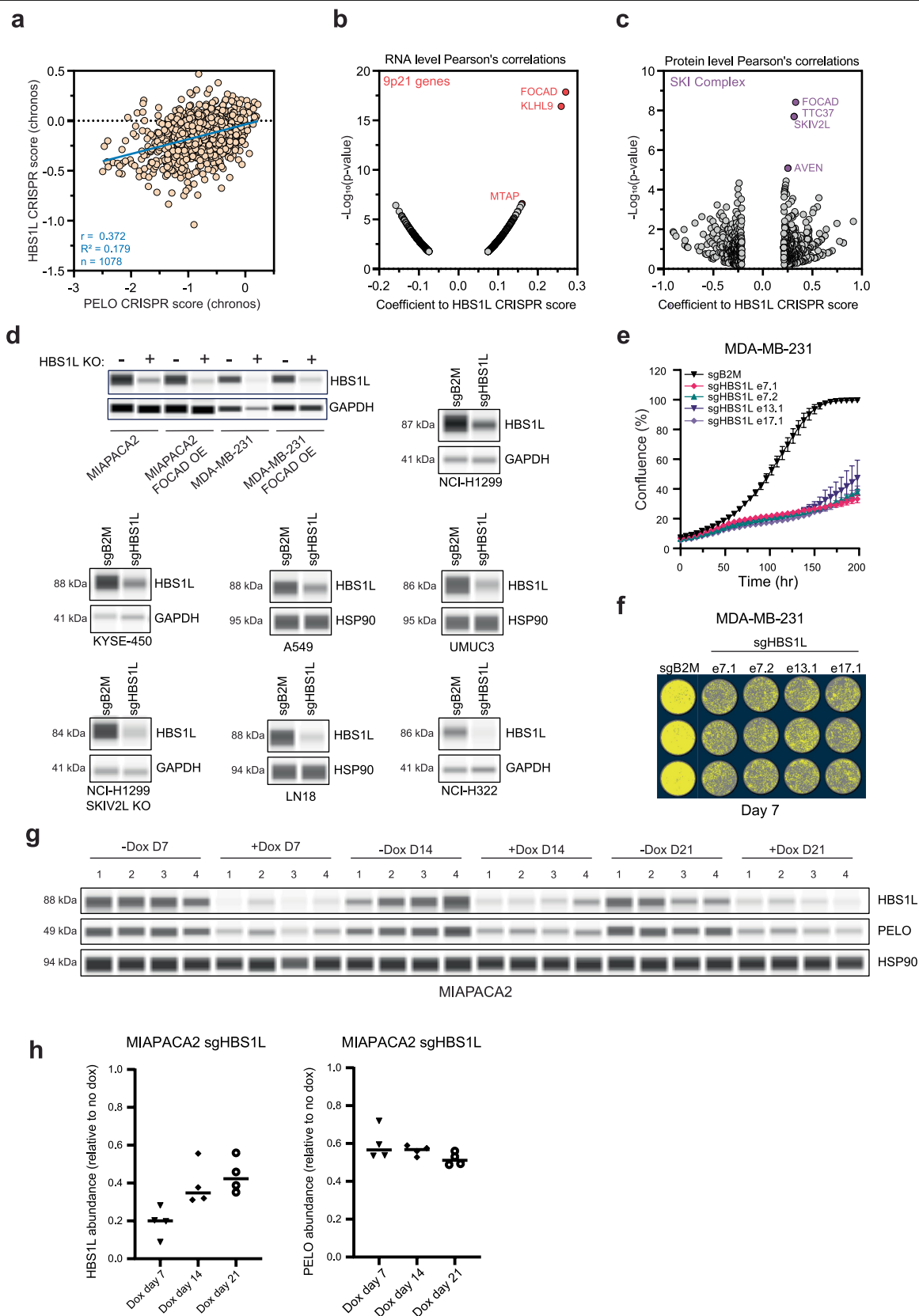
and TTC37 relative protein levels from colorectal CPTAC proteomic data ($n = 96$). MSI-H tumors highlighted in red. Pearson's coefficient of determination, $R^2 = 0.52$. (f) cBioPortal OncoPrint showing mutual exclusivity of *FOCAD* homozygous deletions, *MSH2*, *PMS1*, *PMS2*, *RPL22* mutations across major lineage MSI-H solid tumors (bowel, uterine, endometrial). (g) PELO and WRN dependency comparison across MSI-H ($n = 61$) models by NGS grouped by TP53 LOF or WT status. PELO dependency score (blue), WRN (orange). Median denoted by red line. (h) Relative viability of DLD-1 MSI-H cells after sgPELO, sgWRN, and sgABCE1 on day 7. Data shown as mean \pm s.e.m., $n = 5$ biologically independent replicates (i) Immunoblot validation of sgPELO and sgWRN knockdown efficiency in experiments in (h), data presented is a single representative image from $n = 2$ biologically independent replicates.



Extended Data Fig. 7 | Pathway analysis of PELO/SKI synthetic lethality.

(a) Gating strategy for cell cycle analysis by flow cytometry for cell cycle analysis. (b) Cell cycle analysis by flow cytometry. Scatters of PI, propidium iodide (x-axis) vs. Edu (y-axis) and raw plots for quantification in Fig. 5c. (c) Quantification of cell viability and death markers; calcein blue (blue); apotracker (green); mitotracker (red), in NCI-H1299 and MDA-MB-231 SKIc isogenic models at 72 h post sgPELO transfection. Data shown as mean \pm s.e.m., $n = 3$ biologically independent replicates. (d) Percent Cytotox and Annexin V positive cells 120 h

post sgB2M (grey), sgPELO (blue), sgRAN (red). Data shown as mean \pm s.e.m., $n = 5$ biologically independent replicates. (e) Leading edge plots of highlighted gene expression programs from Fig. 5d. (f) Immunoblot of endogenous 9p21 models 48 h after sgB2M or sgPELO transfection for UPR target genes. Data is representative image from $n = 2$ independent biological replicates. (g) Quantification of percent IRE1 α levels 48 h after sgPELO transfection across $n = 5$ deleted and $n = 7$ wildtype 9p21.3 cell line models. Data shown as mean \pm s.e.m.



Extended Data Fig. 8 | See next page for caption.

Extended Data Fig. 8 | Validation of HBS1L dependency. (a) Correlation of *HBS1L* and *PELO* Chronos scores across DepMap models from 23Q4 release ($n = 1078$). (b) Correlation of *HBS1L* dependency to RNA expression data across all lineages and models. The top 1000 correlated genes are shown. Highlighted 9p21.3 genes in red. P-value calculated by two-tailed Student's *t*-test. (c) Correlation of *HBS1L* dependency to proteomic expression data across all lineages and models. The top 1000 correlated proteins are shown. Highlighted SKIc member proteins shown in purple. P-values calculated by *F*-test. (d) Validation of *HBS1L* knockout in models assessed in Fig. 5a. (e) Confluency over time of MDA-MB-231 cells after transfection of sgB2M or four independent sgRNA's targeting *HBS1L* (e7.1, e7.2, e13.1, e17.1). Data shown as mean \pm s.e.m. of $n = 2$ independent biological replicates. (f) Representative confluency images of MDA-MB-231 cells containing sgB2M control or one of four sgRNA's targeting *HBS1L*. Image acquired on day 7. Representative image of a single replicate of $n = 3$ independent biological experiments. (g) Immunoblot of HBS1L and PELO from in vivo doxycycline sg*HBS1L* study, $n = 4$ tumors harvested at each time-point post dox (D7, D14, D21) for both the no dox and dox conditions. (h) Quantification of HBS1L and PELO after in vivo sg*HBS1L* inducible knockout, normalized to HSP90 loading control. Shown as the mean of $n = 4$ animals per group.

Reporting Summary

Nature Portfolio wishes to improve the reproducibility of the work that we publish. This form provides structure for consistency and transparency in reporting. For further information on Nature Portfolio policies, see our [Editorial Policies](#) and the [Editorial Policy Checklist](#).

Statistics

For all statistical analyses, confirm that the following items are present in the figure legend, table legend, main text, or Methods section.

n/a	Confirmed
<input type="checkbox"/>	<input checked="" type="checkbox"/> The exact sample size (<i>n</i>) for each experimental group/condition, given as a discrete number and unit of measurement
<input type="checkbox"/>	<input checked="" type="checkbox"/> A statement on whether measurements were taken from distinct samples or whether the same sample was measured repeatedly
<input type="checkbox"/>	<input checked="" type="checkbox"/> The statistical test(s) used AND whether they are one- or two-sided <i>Only common tests should be described solely by name; describe more complex techniques in the Methods section.</i>
<input type="checkbox"/>	<input checked="" type="checkbox"/> A description of all covariates tested
<input checked="" type="checkbox"/>	<input type="checkbox"/> A description of any assumptions or corrections, such as tests of normality and adjustment for multiple comparisons
<input type="checkbox"/>	<input checked="" type="checkbox"/> A full description of the statistical parameters including central tendency (e.g. means) or other basic estimates (e.g. regression coefficient) AND variation (e.g. standard deviation) or associated estimates of uncertainty (e.g. confidence intervals)
<input type="checkbox"/>	<input checked="" type="checkbox"/> For null hypothesis testing, the test statistic (e.g. <i>F</i> , <i>t</i> , <i>r</i>) with confidence intervals, effect sizes, degrees of freedom and <i>P</i> value noted <i>Give P values as exact values whenever suitable.</i>
<input checked="" type="checkbox"/>	<input type="checkbox"/> For Bayesian analysis, information on the choice of priors and Markov chain Monte Carlo settings
<input checked="" type="checkbox"/>	<input type="checkbox"/> For hierarchical and complex designs, identification of the appropriate level for tests and full reporting of outcomes
<input type="checkbox"/>	<input checked="" type="checkbox"/> Estimates of effect sizes (e.g. Cohen's <i>d</i> , Pearson's <i>r</i>), indicating how they were calculated

Our web collection on [statistics for biologists](#) contains articles on many of the points above.

Software and code

Policy information about [availability of computer code](#)

Data collection	<div>FloJo 10.8.1 SW Compass v6.2 DRAGEN v4.0 PyMol (v1.7.6.6) HCS Studio Target Activation.V4 Incucyte Satorius v2022B Transcriptomic data was acquired as follows. Total RNA was harvested from cell pellets using RNAeasy columns (Qiagen). Libraries were prepped using the NEB Ultra II RNA library prep kit and sequenced on NextSeq HighOutput 300-Cycle flow cell (2x100bp).</div>
Data analysis	<div>Data was analyzed as follows. Reads were aligned using Illumina DRAGEN v4.0 software. Counts were calculated using featureCounts from subread package and subsequently adjusted with TMM normalization and limma-voom transformation. Differential expression analysis was performed using limma. Gene set enrichment analyses were performed using the fgsea package.</div>

For manuscripts utilizing custom algorithms or software that are central to the research but not yet described in published literature, software must be made available to editors and reviewers. We strongly encourage code deposition in a community repository (e.g. GitHub). See the Nature Portfolio [guidelines for submitting code & software](#) for further information.

Data

Policy information about [availability of data](#)

All manuscripts must include a [data availability statement](#). This statement should provide the following information, where applicable:

- Accession codes, unique identifiers, or web links for publicly available datasets
- A description of any restrictions on data availability
- For clinical datasets or third party data, please ensure that the statement adheres to our [policy](#)

All source data generated was shared as a Supplementary Material or Source Data.

RNA-seq data available through GEO by accession number GSE261804.

Figures 1A and 2C were generated using Biorender: images accessible at BioRender.com/s15m274 and [Biorender.com/x63t552](https://BioRender.com/x63t552).

TCGA Research Network (<https://www.cancer.gov/tcga>) and accessible publicly at cbioportal.org.

Tumor proteomic data by the National Cancer Institute Clinical Proteomic Tumor Analysis Consortium (CPTAC): cbioportal.org

PELO/HBS1L model (Fig 6B) - adapted from: <https://www.rcsb.org/structure/5LZZ>

Field-specific reporting

Please select the one below that is the best fit for your research. If you are not sure, read the appropriate sections before making your selection.

☒ Life sciences ☐ Behavioural & social sciences ☐ Ecological, evolutionary & environmental sciences

For a reference copy of the document with all sections, see nature.com/documents/nr-reporting-summary-flat.pdf

Life sciences study design

All studies must disclose on these points even when the disclosure is negative.

Sample size

No statistical methods were used to predetermine sample sizes but are consistent with previous publications for tumor vulnerability and synthetic lethality.

1. Chan, E. M. et al. WRN Helicase is a Synthetic Lethal Target in Microsatellite Unstable Cancers. *Nature* 568, 551–556 (2019).
2. Gallo, D. et al. CCNE1 amplification is synthetic lethal with PKMYT1 kinase inhibition. *Nature* 604, 749–756 (2022).
3. Kryukov, G. V. et al. MTAP deletion confers enhanced dependency on the PRMT5 arginine methyltransferase in cancer cells. *Science* 351, 1214–1218 (2016).
4. Shi, X. et al. Building a translational cancer dependency map for The Cancer Genome Atlas. *Nat. cancer* 1–19 (2022) doi:10.1038/s43018-024-00789-y.

Data exclusions

No data was excluded from this study.

Replication

Exact n for biological replication is made available in manuscript for each experiment. All attempts at replication were successful.

Randomization

No randomization with exception of at size match of inducible PELO and HBS1L sgRNA MIAPACA2 studies to ensure equivalent tumor volume prior to dox feed

Blinding

The investigators were not blinded during this study.

Reporting for specific materials, systems and methods

We require information from authors about some types of materials, experimental systems and methods used in many studies. Here, indicate whether each material, system or method listed is relevant to your study. If you are not sure if a list item applies to your research, read the appropriate section before selecting a response.

Materials & experimental systems

- | | |
|-------------------------------------|---|
| n/a | Involved in the study |
| <input type="checkbox"/> | <input checked="" type="checkbox"/> Antibodies |
| <input type="checkbox"/> | <input checked="" type="checkbox"/> Eukaryotic cell lines |
| <input checked="" type="checkbox"/> | <input type="checkbox"/> Palaeontology and archaeology |
| <input type="checkbox"/> | <input checked="" type="checkbox"/> Animals and other organisms |
| <input checked="" type="checkbox"/> | <input type="checkbox"/> Human research participants |
| <input checked="" type="checkbox"/> | <input type="checkbox"/> Clinical data |
| <input checked="" type="checkbox"/> | <input type="checkbox"/> Dual use research of concern |

Methods

- | | |
|-------------------------------------|--|
| n/a | Involved in the study |
| <input checked="" type="checkbox"/> | <input type="checkbox"/> ChIP-seq |
| <input type="checkbox"/> | <input checked="" type="checkbox"/> Flow cytometry |
| <input checked="" type="checkbox"/> | <input type="checkbox"/> MRI-based neuroimaging |

Antibodies

Antibodies used	The following primary antibodies were used to detect protein abundance in Simple Western assays: PELO (ProteinTech, 10582-1-AP), HBS1L (ProteinTech, 10359-1-AP), SKIV2L (ProteinTech, 11462-1-AP), TTC37 (Abcam, ab122421), WDR61 (Invitrogen, PA5-59052), FOCAD (Invitrogen, PA5-63051), AVEN (ProSci, 2413), ABCE1 (Abcam, ab185548), JNK (Cell Signaling, 4672), pJNK (Cell Signaling, 4668), p38 (Cell Signaling, 9212), p-p38 (Cell Signaling, 9211), EIF2S1 (Cell Signaling, 5324), p-EIF2S1 (Abcam, ab32157), IRE1α (Cell Signaling, 3294), pIRE1α (Novus Biologicals, NB100-2323), PERK (Cell Signaling, 3192), pPERK (Cell Signaling, 3179), CHOP (ThermoFisher Scientific, MA1-250), c-JUN (Cell Signaling, 9165), p21 (Cell Signaling, 2947), PARP (Cell Signaling, 3898), HSP90 (Cell Signaling, 4877), GAPDH (Cell Signaling, 2118), HiBIT (Promega, N7200). Antibodies were diluted at 1:100 except for HSP90 (1:500), GAPDH (1:3000). High Content antibodies as followed: rabbit anti-IRE1α (Invitrogen PA5-20189), dilution 1:500. Goat anti-Rabbit IgG (H+L) Cross-Adsorbed Secondary Antibody, Alexa Fluor™ 568 (ThermoFisher A-11011), dilution 1:500.
Validation	All antibodies in this study were validated using RNP CRISPR KO of target gene and protein detection at expected molecular weight by Simple Western analysis. PELO, HBS1L, SKIV2L, TTC37, AVEN, FOCAD, ABCE1 antibody validation data available in Supplementary File 1. All other antibodies validated independent figures not included in this manuscript using equivalent RNP KO methodology.

Eukaryotic cell lines

Policy information about [cell lines](#)

Cell line source(s)	MDA-MB-231, NCI-H1299, PC-3, MCF7, HCC38, UMUC3, NCI-H1975, PANC-1, NCI-H460, MDA-MB-468, A549, NCI-H1437, SNU-44948, U118-MG, CAPAN-1, DAOY, MIAPACA-2, NCI-H838, NCI-H1755, LN18, NCI-H747, SW-837, T84, COLO205, COLO201, RKO, DLD-1, SW48, HEMA, TFF-1, ARPE-19, MCF-10A, and HEK-293 cells were purchased from the American Type Culture Collection (ATCC). KYSE-450, MFE-319, COLO678 were purchased from Leibniz Institute DSMZ (DSMZ). U87-MG was acquired from Ludwig Institute. LK-2 was acquired from the Japanese Collection of Research Biosources (JCRB), HT-29 was acquired from the National Institute of Health (NIH) and NCI-H322, HT115, and HT55 were acquired from the European Collection of Authenticated Cell Cultures (ECACC). All cell lines were confirmed for identity by short tandem repeat profiling and confirmed to be negative for mycoplasma. All cell lines were cultured in DMEM or RPMI (Gibco) supplemented with 10% heat inactivated FBS (Gibco).
Authentication	All cell lines were authenticated by short tandem repeat profiling (STR). Data available if requested.
Mycoplasma contamination	All cell lines were confirmed Mycoplasma negative. Data available if requested.
Commonly misidentified lines (See ICLAC register)	No ICLACv12 commonly misidentified lines used in this manuscript

Animals and other organisms

Policy information about [studies involving animals](#); [ARRIVE guidelines](#) recommended for reporting animal research

Laboratory animals	Female, CB17-SCID mice were used for MIA PaCa 2 tumor studies. NSG mice were used for MDA MB 231 tumor studies. SCID-bg mice were used for NCI-H1299 tumor studies. n = 8 mice/group. Mice were randomized by tumor volume into group using a deterministic methodology. Mice were between 6-8 weeks old at study initiation.
Wild animals	No wild animals were used in this study.
Field-collected samples	No field-collected samples were used in this study.
Ethics oversight	All experiments were conducted in compliance with AbbVie's Institutional Animal Care and Use Committee and the NIH Guide for Care and Use of Laboratory Animals guidelines in a facility accredited by the Association for the Assessment and Accreditation of Laboratory Animal Care. A maximum of 2000mm ³ tumor volume was allowed as per institutional guidelines.

Note that full information on the approval of the study protocol must also be provided in the manuscript.

Flow Cytometry

Plots

Confirm that:

- ☒ The axis labels state the marker and fluorochrome used (e.g. CD4-FITC).
- ☒ The axis scales are clearly visible. Include numbers along axes only for bottom left plot of group (a 'group' is an analysis of identical markers).
- ☒ All plots are contour plots with outliers or pseudocolor plots.
- ☒ A numerical value for number of cells or percentage (with statistics) is provided.

Methodology

Sample preparation	we used the Click-iT Edu Alexa Fluor 647 kit, Apotracker green, Calcein Blue, and Mitotracker red (all according to the
--------------------	---

Sample preparation	manufacturers' protocols) to profile the NCI-H1299 and MDA-MB-231 human cancer cell lines.
Instrument	NovoCyte Quanteon
Software	FlowJo 10.8.1
Cell population abundance	No cells were sorted, only populations analyzed
Gating strategy	For all analyses, cells were first gated using SSC-A v. FSC-A to exclude cell debris. Next, we plotted FSC-H v. FSC-A to exclude doublets. For the cell cycle analysis, we gated G1 phase based on low EdU/low PI, S phase based on high EdU/intermediate PI, and G2 phase based on low EdU/high PI. For the cell death panel, we used positive control samples of healthy, WT cells to gate a calcein blue high/mitotracker red high/apotracker low population; these were our viable cells, and cells scattering outside of this gate were deemed low for calcein blue/mitotracker red and high for apotracker green. Gating strategy shown in Extended Data 6A.

☒ Tick this box to confirm that a figure exemplifying the gating strategy is provided in the Supplementary Information.